## Original Article

**Author for correspondence:**
Jinghui Ma,
Email: majinghui10@xju.edu.cn;
Changcheng Han,
Email: hanchangcheng@xju.edu.cn

**CAMBRIDGE**
UNIVERSITY PRESS

# Paleo-trade wind directions over the Yangtze Carbonate Platform during the Cambrian–Ordovician, Southern China

Chenlin Hu[1,2] , Tianyou Qin[1,2], Jinghui Ma[1,2], Changcheng Han[1,2] and Xuliang Wang[1,2]

[1]Xinjiang Key Laboratory for Geodynamic Processes and Metallogenic Prognosis of the Central Asian Orogenic Belt, Xinjiang University, Urumqi 830017, China and [2]School of Geology and Mining Engineering, Xinjiang University, Urumqi 830017, China

## Abstract

The Sichuan Basin was a part of the Yangtze Carbonate Platform (YCP) during the Cambrian–Ordovician, and marine carbonates were deposited in the basin during this interval. Although previous studies have evaluated the paleogeography, paleoclimate and paleoecology of this basin, they have primarily focused on the paleoecology and biological evolution in the basin; however, analysis of paleogeography and paleoclimate is lacking. This study integrated outcrop sedimentological and magnetic fabric data to document sedimentary differentiation and anisotropy of magnetic susceptibility (AMS) within the YCP. The aims of this study were to infer paleowind directions during each epoch of the Cambrian–Ordovician and to constrain the paleogeographic location of the YCP. The northwestern, central and southeastern sides of the YCP were characterized by high-energy deposition (e.g. sub-angular to rounded intraclasts), medium-energy deposition (e.g. sub-angular to sub-rounded intraclasts) and low-energy deposition (e.g. angular to sub-angular intraclasts), respectively. The centroid D-$K_{max}$ values for the Early, Middle and Late Cambrian were $116° ± 52°$, $145° ± 57°$ and $159° ± 62°$ from the present north, respectively; corresponding values for the Early, Middle and Late Ordovician were $169° ± 70°$, $139° ± 73°$ and $91° ± 68°$ from the present north, respectively. Sedimentary differentiation and AMS results indicated that the prevailing wind directions during the Early Cambrian, Middle Cambrian, Late Cambrian, Early Ordovician, Middle Ordovician and Late Ordovician were $296° ± 52°$, $325° ± 57°$, $339° ± 62°$, $349° ± 70°$, $319° ± 73°$ and $271° ± 68°$ from the present north, respectively. The present study provides evidence for the location of the YCP during the Cambrian–Ordovician via the correspondence between the paleowind directions over the YCP and the trade winds in the Northern and Southern hemispheres. The novelty of this study lies in the following aspects: (1) it integrates microfacies and AMS analyses to establish paleowind patterns; (2) it constrains the paleohemispheric location of the YCP during the Cambrian–Ordovician; and (3) it provides a reference for further studies of the paleoclimate and paleogeography of the YCP during the Cambrian–Ordovician.

## 1. Introduction

Carbonate platform sediments undergo sedimentary differentiation under the action of long-term prevailing winds (Han *et al.* 2020; Hu *et al.* 2020a, 2020b; Hu *et al.* 2022). Anisotropy of magnetic susceptibility (AMS) has been widely used as an indicator of paleowind or paleocurrent directions (Lagroix & Banerjee, 2002; Nawrocki *et al.* 2018; Hu *et al.* 2020a, 2020b). Hydrodynamic experiments have demonstrated the influence of wind or water motion on grain orientation (Rees & Woodall, 1975; Tarling & Hrouda, 1993; Hu *et al.* 2017; Zhang-YF *et al.* 2017; Zhang-YF *et al.* 2018). Under calm conditions, the maximum AMS axes are randomly distributed. Under a strong unidirectional flow, oblate particles tend to produce an imbricate fabric in the direction of the flow and elongated particles are aligned parallel to the direction of transport. Under bidirectional flow, elongated grains may align perpendicular to the directions of fluid movement (Rees & Woodall, 1975; Tarling & Hrouda, 1993; Hu *et al.* 2017). This study reconstructed paleowind directions during each epoch of the Cambrian–Ordovician the Yangtze Carbonate Platform (YCP) using sedimentary differentiation and AMS analysis.

The YCP was located in the low-latitude trade winds belt during the Cambrian–Ordovician, and marine carbonates were deposited there (Li *et al.* 2015; Zhang *et al.* 2019; Cheng *et al.* 2020). Like other platforms, the YCP was subjected to extensive global transgression during the Cambrian (Dalziel, 2014; Chang *et al.* 2018; Zhai *et al.* 2018; Wu *et al.* 2021). The water in the ocean was warm and conducive to the growth and development of marine organisms (Peters & Gaines, 2012; Karlstrom *et al.* 2018; Wood *et al.* 2019). Numerous organisms began

to emerge during this time, and some primitive invertebrates gradually evolved into invertebrates with hard shells; this phenomenon is known as the 'Cambrian Explosion' (Jin *et al.* 2016; Aria & Caron, 2019; Hoyal Cuthill *et al.* 2020). As part of the most extensive transgression in the Early Paleozoic, conditions during the Ordovician favoured the further development of invertebrates (Kröger, 2018; Stigall *et al.* 2019; Fang *et al.* 2020; Harper *et al.* 2021). The paleoecology and biological evolution of the YCP during the Cambrian–Ordovician have been extensively investigated (e.g. Li *et al.* 2015; Lee & Riding, 2018; Zheng *et al.* 2020), but studies on its paleogeography and paleoclimate are scarce (e.g. Torsvik & Cocks, 2013; Zhang *et al.* 2016; Cocks & Torsvik, 2021). The paleogeography and paleoclimate influence paleoecology and biological evolution in a region, and therefore, it is necessary to comprehensively understand these aspects.

Most scholars hold that the YCP was located in low-latitude area of the Northern and Southern hemispheres during the Cambrian–Ordovician. Some scholars hold that the YCP drifted from the Southern Hemisphere (~12°S) to the Northern Hemisphere (~11°N), then back to the Southern Hemisphere (~49°S), and finally drifted to the Northern Hemisphere (~7°N) from the Middle Cambrian to the Middle Ordovician (e.g. Huang *et al.* 2000). Other scholars believe that the platform first drifted southward across the equator from the Northern Hemisphere (~13°N) to the Southern Hemisphere (~28°S) and then drifted northward to a location near the equator from the Early Cambrian to the Late Ordovician (e.g. Torsvik & Cocks, 2013; Cocks & Torsvik, 2021). The paleogeographic constraints (paleomagnetic or otherwise) are testable based on the expected paleoclimate conditions, especially the paleowind directions. The paleo-coordinate framework during the Cambrian–Ordovician in the trade wind belt indicates that the prevailing winds in the Northern and Southern hemispheres at the time were from northeast and from southeast, respectively (Kajtar *et al.* 2018; Helfer *et al.* 2020, 2021). On the whole, there is no consensus regarding the specific paleogeographic site and orientation of the YCP (Huang *et al.* 2000; Popov *et al.* 2009; Nardin *et al.* 2011; Torsvik & Cocks, 2013; Cocks & Torsvik, 2021; Harper *et al.* 2021). These conflicting proposals emphasize the need to reconstruct paleowind directions.

The present study conducted an integrated analysis of bed- to platform-scale variations in sediments based on outcrop data to quantitatively reconstruct paleowind directions. One novel feature of the present study is the inclusion of quantitative measurements of sediment properties potentially influenced by the wind and wind-generated currents, such as bedding thickness and grain size and sorting, across the YCP. The aims of the present study were to (1) quantitatively reconstruct paleowind directions over the YCP during the Cambrian–Ordovician and (2) constrain the paleogeographic location of the YCP. The results of the present study can serve as a reference for the integrated use of sedimentological and AMS data for the recognition of paleowind directions over ancient carbonate platforms.

## 2. Geological setting

The Sichuan Basin is a gas-bearing superimposed basin (with complex structure due to vertical stacking of different structural layers) that occupies an area of ~$1.9 \times 10^5$ km². It is mainly distributed in Sichuan Province and Chongqing City, the southern part of Shaanxi, eastern portion of Guizhou and western part of Hubei.

The basin is bounded by the Micang and Daba mountains in the north, the Daliang and Loushan mountains in the south, the Longmen Mountains in the west and Qiyao Mountain in the east (Liu *et al.* 2021; Cheng *et al.* 2022; Dong *et al.* 2022). The Sichuan Basin is situated on a basement of pre-Sinian metamorphic and igneous rocks and contains marine and continental strata with the thickness of 6–12 km (Shi *et al.* 2020; Zhao *et al.* 2020; Miao *et al.* 2022). This study primarily focused on marine carbonate deposits in the YCP region, where the Sichuan Basin was located during the Cambrian–Ordovician (Figs. 1, 2).

### 2.a. Tectonic setting

The Sichuan Basin was in an extensional tectonic setting from the Late Sinian to the Early Cambrian, during which time the Tongwan tectonic event established the paleogeomorphic framework of this basin (Wang *et al.* 2014; Che *et al.* 2019; Zhou *et al.* 2020). This tectonic event caused the episodic uplift of the crust, and each portion of this basin underwent varying degrees of uplift and subsidence; furthermore, the platform region underwent several episodes of denudation, which occurred in varying degrees. Moreover, under the influence of the extensional regime, the Deyang-Anyue Rift Tough developed in the western area, and the region as a whole exhibited a north–south-oriented uplift and depression pattern (Liu *et al.* 2017; Jin *et al.* 2020; Li *et al.* 2020). The Deyang-Anyue Rift Trough formed due to the early tectonic event and entered a stage of compensatory deposition. The basin was filled with a set of thick-bedded deposits dominated by shales whose sedimentary provenance indicated that they originated from the west and north (Liu *et al.* 2020; Zhao *et al.* 2020; Wang *et al.* 2021).

During the deposition of the Canglangpu Formation, the amplitude of vertical tectonic event decreased considerably, the uplift and depression pattern began to disappear, and the basin paleogeomorphology gradually transformed from the pattern of alternating uplift and depression to that of a shelf with a gentle slope from west to east. The Canglangpu Formation, which consists of sandy shale mixed with limestone and dolostone, was deposited in this environment. During the Middle-Late Cambrian, this area was characterized by semi-restricted and restricted lagoon; the seawater receded and the paleo-uplift further developed during this time. From the Douposi Formation, the depositional environment gradually changed to a carbonate platform (Figs. 1, 2; Fu *et al.* 2020; Li *et al.* 2021; Zhang *et al.* 2022).

The Sichuan Basin is dominated by carbonate deposits; it was covered by a wide epicontinental sea from the Early to the Late Ordovician (Zhu *et al.* 2018; He *et al.* 2019; Yang *et al.* 2022). Owing to the Guangxi tectonic event, the convergence of the block intensified, and the Yangtze Block was subducted and compressed by the Cathaysia Block in the southeast (Ge *et al.* 2019; Wang *et al.* 2019; Huang *et al.* 2020). The surrounding paleo-lands of the Sichuan Basin were uplifted. The Qianzhong Paleo-land was connected with Xuefeng Paleo-land. The Kangdian and Chuanzhong paleo-lands were expanded. At this juncture, the passive continental margin began to transform into a foreland basin, low-energy and undercompensated depositional basins enclosed by uplifts began to form within the plate (Wang *et al.* 2019; Men *et al.* 2020; Lu *et al.* 2021). Lithofacies analysis indicated that the carbonate deposits were replaced by terrigenous clastic deposits. The early limestone deposits of the Baota and Linxiang formations were overlain by the black shale deposits of the Wufeng and Longmaxi formations from the Late Ordovician to the Early
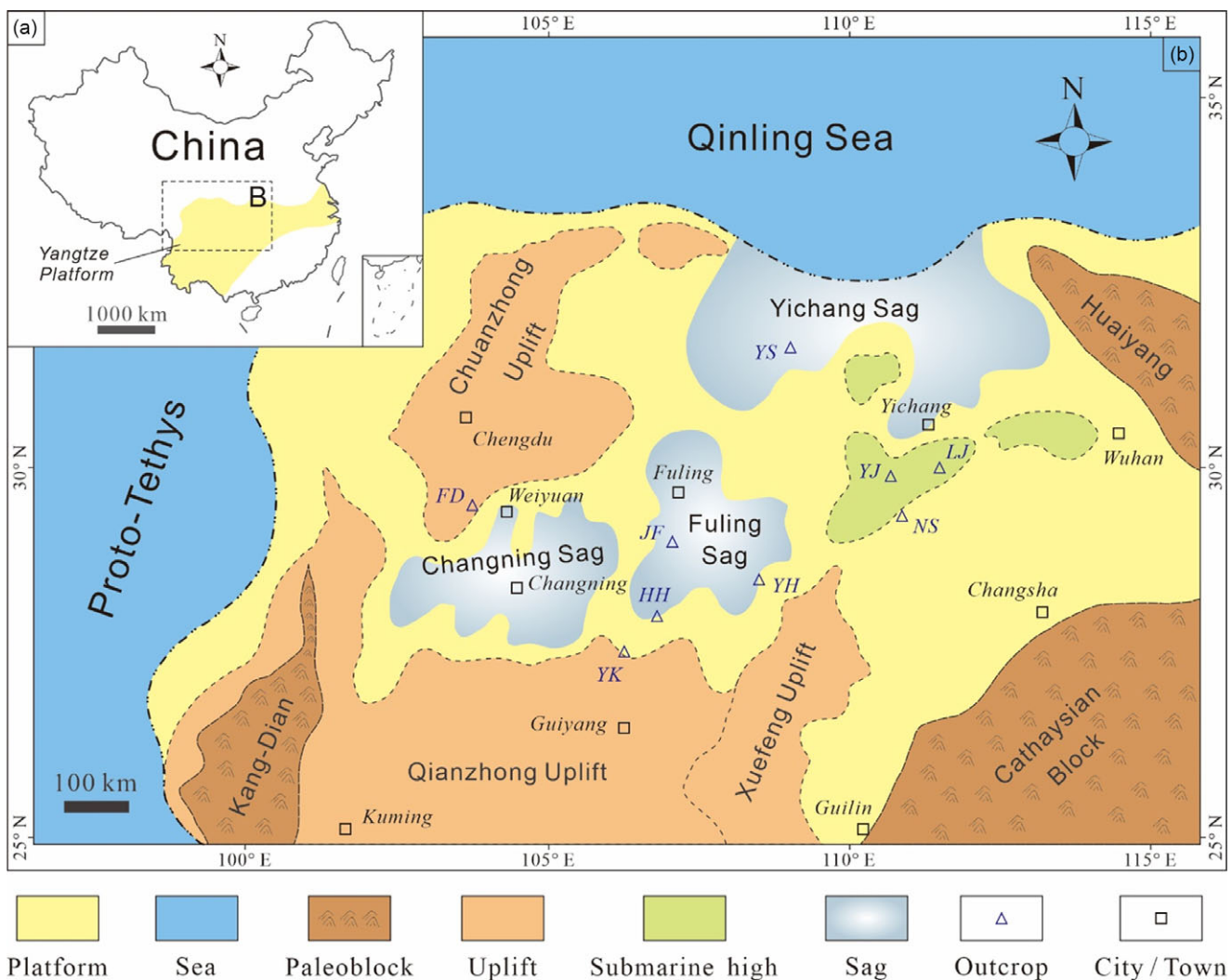
**Fig. 1.** (Colour online) Regional index map showing the study area. (a) Simplified map of China showing the location of the YCP (after Chen *et al.* 2004). (b) Paleogeographic map of the YCP during the Late Ordovician, showing the outcrop locations used in the present study (after Chen *et al.* 2004). Detailed information of the nine outcrops (LJ, FD, YK, YS, NY, YJ, HH, JF, NS and YH) is provided in Table S1.

Silurian (Figs. 1, 2; Chen *et al.* 2004; Liang *et al.* 2012; Huang *et al.* 2020).

### 2.b. Stratigraphy

The Cambrian–Ordovician strata in the Sichuan Basin and its adjacent areas differ greatly in different regions. The Cambrian strata are dominated by terrigenous clastic deposits in the west and marine carbonate deposits in the east (Wang *et al.* 2013; Zhang *et al.* 2019; Xi *et al.* 2022). The thickness of the Cambrian succession is ~100–1500 m, whereas the strata in the western part of the basin are thinner (~100–500 m) because of the later denudation. The strata in the central part of the basin have a medium thickness of ~500–1200 m. The strata in the eastern part of the basin are thicker, reaching ~1500 m (Liu *et al.* 2018; Li *et al.* 2022; Wang *et al.* 2022). The western area contains the Lower Cambrian Dengying, Qiongzhusi, Canglangpu and Longwangmiao formations, the Middle Cambrian Gaotai Formation and the Upper Cambrian Xixiangchi Formation from bottom to top. Thick layers of shale, clastic rock and various carbonate rocks have been deposited (Yang *et al.* 2012; Gu *et al.* 2015; Gao *et al.* 2021).

The Ordovician strata have inherited the characteristics of the Cambrian succession, with the depositional basement being high in the west and low in the east, and the sediments being coarse in the west and fine in the east. The stratigraphic thickness of the Ordovician succession is less than that of the Cambrian succession. The stratigraphic thickness of the Ordovician succession is ~0–800 m; the Ordovician strata have undergone denudation, especially in the western part of the basin (Wang *et al.* 2016; Zhu *et al.* 2018; Yang *et al.* 2022). The western area contains the Lower Ordovician Tongzi and Honghuayuan formations, the Middle Ordovician Meitan and Shizipu formations and the Upper Ordovician Baota, Linxiang and Wufeng formations from bottom to top. A succession of carbonate rocks, mixtites and shales has been deposited here (Figs. 1, 2; Yang *et al.* 2012; Zhu *et al.* 2021; Miao *et al.* 2022).

### 2.c. Carbonate microfacies and depositional environments

Several depositional environments, such as restricted platform, open platform and platform margin, are seen in the Cambrian–Ordovician system (Yang *et al.* 2012; Li *et al.* 2013; Zhang *et al.*

| System | Series | Stage | Western Region | Leibo Region | Nanjiang Region | Eastern Region | Chengkou Region |
|---|---|---|---|---|---|---|---|
| Ordovician | Upper | Hirnantian | Wufeng | Wufeng | Wufeng | Wufeng | Wufeng |
| | | Qiantangjiangian | Linxiang | Linxiang | Linxiang | Linxiang | Linxiang |
| | | Aijiashanian | Baota | Baota | Baota | Baota | Baota |
| | | | | | | | Miaopo |
| | Middle | Darriwilian | *Lacunna* / Shizipu | Qiaojia | Tanjiagou | Shizipu | Guniutan |
| | | Dapingian | Dachengsi / Meitan | Hongshiya | Xiliangsi | Meitan | Dawan |
| | Lower | Daobaowanian | | | Zhaojiaba | | |
| | | | Honghuayuan | | | Honghuayuan | Honghuayuan |
| | | Xinchangian | Luohanpo / Tongzi | *Lacunna* | *Lacunna* | Tongzi | Fenxiang |
| | | | | | | | Nanjinguan |
| Cambrian | Upper | Fengshanian | Xixiangchi | Erdaoshui | *Lacunna* | Maotianba | Sanyoudong |
| | | Changshanian | | | | Houba | |
| | | Gushanian | | | | | |
| | Middle | Zhangxian | | Xiwangmiao | | Pingjing | Tanjiamiao |
| | | Xuzhuangian | | | | Shilengshui | |
| | | Maozhuangian | Douposi | Douposi | Douposi | Gaotai | |
| | Lower | Longwangmiaoan | Longwangmiao | Longwangmiao | Kongmingdong | Qingxudong / Shilongdong | Shilongdong |
| | | Canglangpuan | Canglangpu | Canglangpu | Yanwangbian | Jindingshan / Tianheban | Tianheban |
| | | | | | Xiannvdong | Mingxinsi / Shipai | Shipai |
| | | Qiongzhusian | Qiongzhusi | Qiongzhusi | Guojiaba | Niutitang / Shuijingtuo | Shuijingtuo |
| | | Meishucunian | | | | *Lacunna* | |
| | | | Dengying | Dengying | Dengying | Dengying / Dengying | Dengying |

**Fig. 2.** (Colour online) Cambrian–Ordovician stratigraphy in the Sichuan Basin area of the YCP (after Yang *et al.* 2012).

2016; Zeng *et al.* 2018). The restricted platform can be divided into three subtypes (tidal flat, lagoon and intraplatform shoal); it is mainly developed in the Lower Cambrian Longwangmiao Formation, the Middle Cambrian Gaotai Formation and the Upper Cambrian Xixiangchi Formation. The rocks of this depositional environment primarily consist of light grey-dark grey micritic dolomite, sandy dolomite and argillaceous dolomite, along with doloarenite, dolorudite, oolitic dolomite and gypsum dolomite (Li *et al.* 2012; Liu *et al.* 2018; Wang *et al.* 2022).

The open platform, which is developed in the Cambrian–Ordovician system, can be divided into the intraplatform shoal and intershoal marine subtypes. The deposits consist of medium-thick stratified light grey and grey micritic limestone, oolitic limestone, argillaceous limestone and intraclastic and bioclastic limestone. The intraplatform shoal subtypes can be divided into sand shoals, oolitic shoals and bioclastic shoals. The intershoal marine subtypes is a relatively low-energy region between intraplatform shoals of the open platform. The sedimentary rocks are dominated by grey and dark grey thin to medium-thick stratified micritic limestone, along with argillaceous limestone, mud-bearing limestone and bioclastic micritic limestone. Moreover, horizontal bedding is developed and foraminifers, bivalves, gastropods and other biogenic fossils are seen (Yang *et al.* 2012; Li *et al.* 2019; Ren *et al.* 2019).

The platform margin is mainly developed in the Ordovician and is distributed along the eastern margin of the Sichuan Basin. The beds are thicker than those of other belts, and the deposits in this region primarily consist of oolitic limestone, oolitic dolomite,

micrite dolomite, arenaceous limestone and small amounts of micritic limestone. The platform margin shoal often shows a convex up shape in the vertical plane because of its rapid growth (Figs. 1, 2; Zhao *et al.* 2014; Zhao *et al.* 2017; Gu *et al.* 2021).

## 3. Sampling and methods

### 3.a. Field methods and sample collection

A total of nine field sites in the Sichuan Basin [the Liujiachang (LJ), Fandian (FD), Yankong (YK), Yangsiqiao (YS), Yangjiaping (YJ), Honghuayuan (HH), Jinfoshan (JF), Nanshanping (NS) and Yanhe (YH) outcrops] were investigated (Fig, 1b). A total of 390 samples were collected at ~17 m intervals through the 1130 m thick Shuijingtuo-Linxiang formations at the LJ site, the 650 m thick Qiongzhusi-Xixiangchi formations at the FD site, the 820 m thick Niutitang-Maotianba formations at the YK site, the 270 m thick Shuijingtuo-Sanyoudong formations at the YS site, the 2330 m thick Niutitang-Maotianba formations at the YJ site, the 440 m thick Tongzi-Wufeng formations at the HH site, the 300 m thick Tongzi-Wufeng formations at the JF site, the 520 m thick Tongzi-Baota formations at the NS site and the 170 m thick Tongzi-Wufeng formations at the YH site (Fig. 2). Detailed field descriptions were made at each site, and numerous measurements and outcrop photographs were obtained. Thin sections of the samples collected at each site were prepared for petrographic analysis (Table S1).

### 3.b. Microfacies analysis

A total of 390 outcrop samples were prepared for thin-section analysis and examined on a standard petrographic microscope (Carl Zeiss Axio Scope A1) using transmitted light microscopy (Table S1). The samples were impregnated with blue resin to highlight porosity and stained with Alizarin Red S for carbonate mineral determination. Mineral identification procedures followed the Rock Thin-Section Identification Standard SY/T 5368-2016 (Luo *et al.* 2016). Grain content was calculated by point counting using a $20 \times 30$ grid ($n = 600$ observations per sample). For particulate sediments (i.e. grainstones), sediment properties such as grain size, roundness and sorting were quantified (Tables S2–S5; Zhou *et al.* 2018; Hu *et al.* 2021; Tang *et al.* 2022; Hu *et al.* 2023b). Samples were evaluated using standard descriptive and interpretative criteria (Wilson *et al.* 1990; Wright, 1992; Tucker & Wright, 2009; Flügel, 2013). Sedimentary differentiation analysis conducted in the present study was based on observations of lithology, bedding, sedimentary textures and grain types (including size, roundness and sorting properties) in outcrops and thin sections.

### 3.c. Magnetic fabric analysis

A total of 1399 fresh samples for magnetic fabric analysis were collected at ~5 m intervals using a portable mini-core drill (D026-C) and an insertable magnetic compass. Magnetic samples were taken from all nine field sites (LJ = 274, FD = 140, YK = 149, YS = 133, YJ = 137, HH = 139, JF = 144, NS = 135 and YH = 148) (Fig. 1b; Table S1). Each core sample had a diameter of 25 mm and was trimmed to a length of 22 mm to maintain a uniform sample volume. After preparation, the magnetic susceptibility of each sample was measured using a magnetic susceptibility metre [HKB-1 (High-accuracy Kappa Bridge-1); field strength: 300 A/m; field frequency: 920 Hz; power: AC, 220 V/110 V, 50/60 Hz and 15 W;

sensitivity: $2 \times 10^{-12}$ m³] with an automated sample handling system. Each sample was measured three times along orthogonal planes.

AMS analyses are used to study variations in the magnetic susceptibility field of a sample within a three-dimensional (3D) orthogonal framework (Lagroix & Banerjee, 2004; Zhang *et al.* 2010; Zhao *et al.* 2023). The AMS of a sample is typically reported in terms of $K_{max}$, $K_{int}$ and $K_{min}$ values, representing the lengths of the maximum, intermediate and minimum principal axes of the 3D AMS ellipsoid, respectively; D-$K_{max}$, D-$K_{int}$ and D-$K_{min}$ values, representing their respective declinations; and I-$K_{max}$, I-$K_{int}$ and I-$K_{min}$ values, representing their respective inclinations. Superposition of ferromagnetic, paramagnetic and diamagnetic grain properties yields the total AMS signal (Zhu *et al.* 2004; Nawrocki *et al.* 2018).

The values of $K_{max}$, $K_{int}$ and $K_{min}$ can be combined in various ways to describe the ellipsoid shape and features of the magnetic fabric of a sample (Jelinek, 1981; Lagroix & Banerjee, 2004; Gong *et al.* 2015). The magnetic parameters developed for this purpose are as follows:

$$\text{Lineation(L)} = K_{max}/K_{int} \tag{1}$$

$$\text{Foliation(F)} = K_{int}/K_{min} \tag{2}$$

$$\text{Degree of anisotropy(P)} = K_{max}/K_{min} \tag{3}$$

$$\text{Shape factor(T)} = (2\eta 2 - \eta 1 - \eta 3)/(\eta 1 - \eta 3) \tag{4}$$

where η1, η2 and η3 are ln ($K_{max}$), ln ($K_{int}$) and ln ($K_{min}$), respectively.

The parameters $F_{12}$ and $F_{23}$, which are used to evaluate the statistical significance of the lineation and the foliation, were determined following the technique of Lagroix and Banerjee (2004) using (1) epsilon $\epsilon_{12}$, the half-angle uncertainty of $K_{max}$ in the plane joining $K_{max}$ and $K_{int}$, and (2) epsilon $\epsilon_{23}$, the half-angle uncertainty of $K_{int}$ in the plane joining $K_{int}$ and $K_{min}$. All of the above parameters were calculated using the Safyr and Anisoft software packages (Constable & Tauxe, 1990).

The geographic orientations of the principal AMS axes were plotted on stereonets for visualization. The sample set was then screened to isolate the most significant $K_{max}$ declination using the technique of Lagroix and Banerjee (2004) and Zhu *et al.* (2004). All D-$K_{max}$ with $F_{12} < 4$ and $\epsilon_{12} > 22.5°$ were rejected to eliminate noise. Rejection of samples with $F_{12} < 4$ yielded a confidence ratio of 1.0 for the intermediate and minimum susceptibility axes of the lineation axis, and rejection of samples with $\epsilon_{12} > 22.5°$ yielded a confidence ratio of 1.0 for the maximum and intermediate susceptibility axes in the foliation plane. I-$K_{min}$ was another parameter used in screening AMS data; values of I-$K_{min} > 70°$ generally correspond to undisturbed (low degree of reworking) sediments with an oblate magnetic fabric (Lagroix & Banerjee, 2004; Nawrocki *et al.* 2018; Hu *et al.* 2020a, 2020b).

## 4. Results

### 4.a. Sedimentary differentiation

Previous studies reported on the general microfacies analysis of Cambrian–Ordovician carbonate facies in the YCP (e.g. Zou *et al.* 2017; Tan *et al.* 2018; Zhang-SC *et al.* 2018; Zhai *et al.* 2019; Fu *et al.* 2020; Gao *et al.* 2021). The present study focused
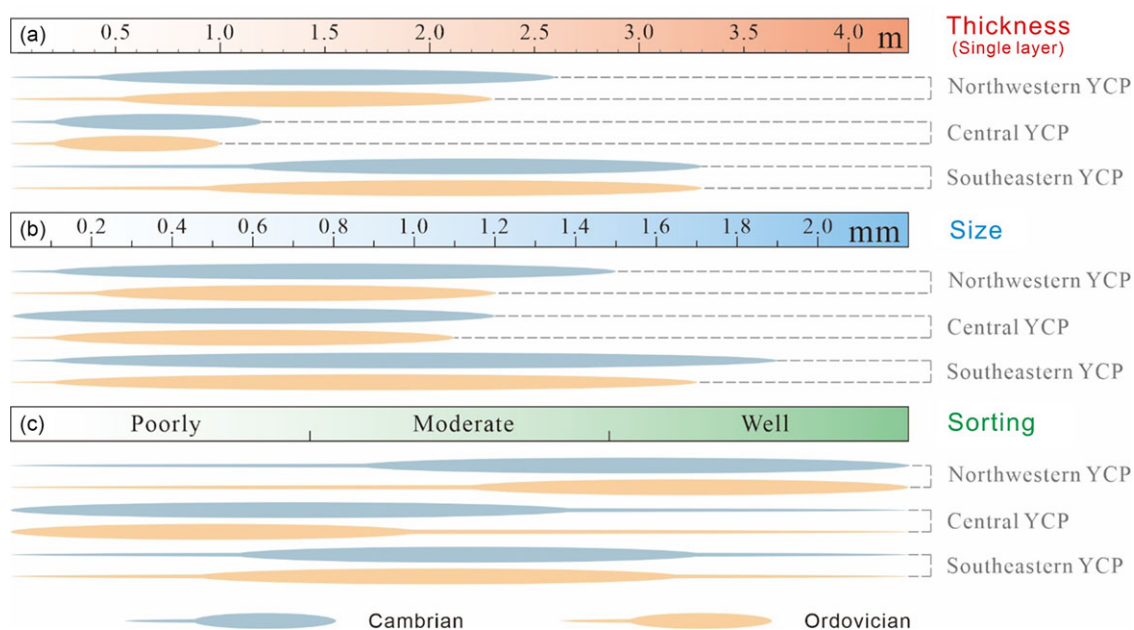
**Fig. 3.** (Colour online) Diagram summarizing the variations in the approximate bedding thickness (a), ooid size (b) and sorting (c) of Cambrian–Ordovician oolitic grainstone.

on oolitic and intraclastic grainstones with the aim of identifying sedimentary differentiation due to prevailing wind directions.

### 4.a.1. Oolitic grainstone

The northwestern, central and southeastern portions of the YCP exhibited differences in the thicknesses of oolitic grainstone beds as well as in the size and sorting of ooids (Fig. 3; Tables S2, S3). The northwestern margin is characterized by moderately sorted to well-sorted ooids that accumulated in a northwest-facing windward environment. In contrast, the southeastern margin shows poorly to moderately sorted sediments (Table 1; Fig. 3). The energy levels at the northwestern margin were relatively high, whereas those at the southeastern margin were relatively low. The southeastern margin has greater bedding thicknesses and ooid grain diameters, and it is inferred to have possessed the optimal growth environment for ooids (Zhang-YY *et al.* 2017; Hu *et al.* 2020a).

### 4.a.2. Intraclastic grainstone

Quantitative measurements of intraclastic grainstone samples from the Cambrian–Ordovician indicated differences in the thickness of intraclastic grainstone beds, as well as in the size, roundness and sorting of intraclasts among the northwestern, central and southeastern regions of the YCP (Fig. 4; Tables S4, S5). The northwestern margin is characterized by moderately sorted to well-sorted and sub-angular to rounded intraclasts that accumulated in a northwest-facing windward environment. In contrast, the southeastern margin shows poorly to moderately sorted sediments with angular to sub-rounded grains (Table 1; Fig. 4). The energy levels at the northwestern margin were relatively high, whereas those at the southeastern margin were relatively low (Hu *et al.* 2020a, 2020b; Hu *et al.* 2023a).

### 4.b. AMS

Most of the samples collected at all locales in the present study exhibited an oblate magnetic fabric (Fig. 5a, b, Figures S2–S3; Lagroix & Banerjee, 2004; Hu *et al.* 2020a, 2020b). The observed ratio of the degree of anisotropy (P) to foliation (F) was consistent with a subordinate role for lineation (L) (Fig. 5c, Figure S4). These features are typical of sediments deposited by wind or water currents (Lagroix & Banerjee, 2004; Nawrocki *et al.* 2018). Inverse relationships were observed between $\epsilon_{12}$ and L (Fig. 5d, Figure S5) and between $\epsilon_{23}$ and F (Fig. 5e, Figure S6), which resulted from increased measurement errors for weak lineations and foliations, respectively. In contrast, the absence of a correlation between $\epsilon_{12}$ and F suggested that the lineation and foliation subfabrics were probably defined by the orientations of different minerals (Fig. 5f, g, Figures S7–S8).

### 4.b.1. AMS for each Cambrian series

The robustness of statistical calculations was increased by limiting calculations to Cambrian samples, for which $F_{12} > 4$, $\epsilon_{12} < 22.5°$ and $I\text{-}K_{min} > 70°$ (Table 2; Fig. 6, Figure S9). The screened sample sets of each Cambrian series yielded $K_{max}$ values with different preferred orientations for each of the five target outcrops (Table 3; Fig. 6, Figure S9). A centroid statistical approach was applied in the Safyr and Anisoft software to assess the distribution of $K_{max}$ values for the screened sample set of each outcrop. This approach was used to determine the dominant orientations. When the inclination is not considered, the centroid statistical diagram only magnifies variations in $K_{max}$ declinations. The centroid $D\text{-}K_{max}$ values of the Lower Cambrian samples were 116° at LJ, 119° at FD, 117° at YK, 115° at YS and 113° at YJ. The centroid $D\text{-}K_{max}$ values of the Middle Cambrian samples were 141° at LJ, 146° at FD, 143° at YK, 149° at YS and 146° at YJ. The centroid $D\text{-}K_{max}$ values of the Upper Cambrian samples were 158° at LJ, 159° at FD, 160° at YK, 161° at YS and 157° at YJ (modern coordinates; Table 3; Fig. 6, Figure S9).

**Table 1.** Comparison of the main sedimentary characteristics for different Cambrian–Ordovician sites

| Sites | Microfacies | Main sedimentary features | |
| --- | --- | --- | --- |
| | | Cambrian | Ordovician |
| Northwestern YCP | Oolitic grainstone | Bed thickness = 1.5 ± 1.1 m; moderate to well-sorted ooids; ooid size = 0.8 ± 0.7 mm | Bed thickness = 1.4 ± 0.9 m; moderate to well-sorted ooids; ooid size = 0.7 ± 0.5 mm |
| | Intraclastic grainstone | Bed thickness = 1.7 ± 1.3 m; moderate to well-sorted and sub-angular to rounded intraclasts; intraclast size = 2.5 ± 1.7 cm | Bed thickness = 1.8 ± 1.4 m; moderate to well-sorted and sub-angular to rounded intraclasts; intraclast size = 2.5 ± 1.5 cm |
| Central YCP | Oolitic grainstone | Bed thickness = 0.7 ± 0.5 m; poorly to moderate sorted ooids; ooid size = 0.6 ± 0.6 mm | Bed thickness = 0.6 ± 0.4 m; poorly to moderate sorted ooids; ooid size = 0.6 ± 0.5 mm |
| | Intraclastic grainstone | Bed thickness = 1.2 ± 0.9 m; moderate sorted and sub-angular to sub-rounded intraclasts; intraclast size = 1.7 ± 1.1 cm | Bed thickness = 1.3 ± 0.8 m; moderate sorted and sub-angular to sub-rounded intraclasts; intraclast size = 1.5 ± 0.9 cm |
| Southeastern YCP | Oolitic grainstone | Bed thickness = 2.2 ± 1.1 m; moderate sorted ooids; ooid size = 1.0 ± 0.9 mm | Bed thickness = 2.1 ± 1.2 m; moderate sorted ooids; ooid size = 0.9 ± 0.8 mm |
| | Intraclastic grainstone | Bed thickness = 0.6 ± 0.5 m; poorly to moderate sorted and angular to sub-rounded intraclasts; intraclast size = 0.8 ± 0.7 cm | Bed thickness = 0.7 ± 0.5 m; poorly to moderate sorted and angular to sub-rounded intraclasts; intraclast size = 0.7 ± 0.6 cm |
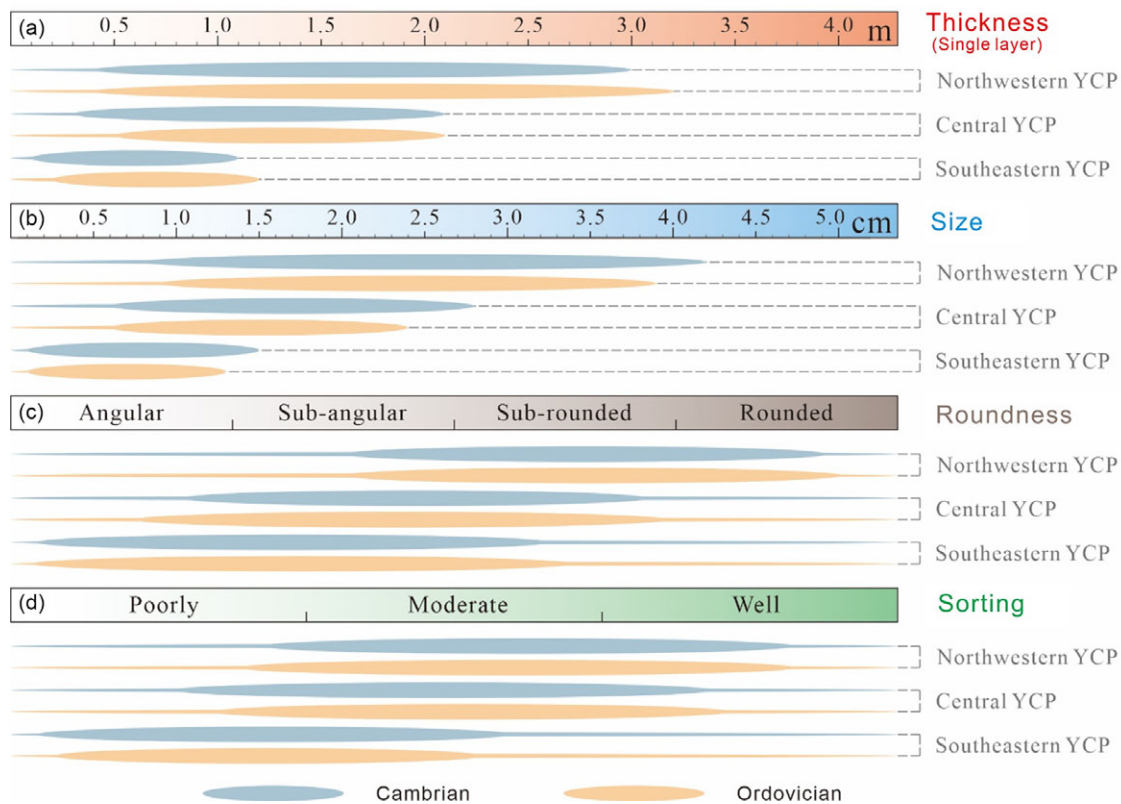


**Fig. 4.** (Colour online) Diagram summarizing the variations in approximate bedding thickness (a), intraclast size (b), roundness (c) and sorting (d) of the Cambrian–Ordovician intraclastic grainstone.

### 4.b.2. *AMS for each Ordovician series*

Statistical robustness was ensured in the present study by limiting calculations to samples of the Ordovician, for which $F_{12} > 4$, $\epsilon_{12} < 22.5°$ and $I\text{-}K_{min} > 70°$ (Table 4; Fig. 7, Figure S10). The screened sample sets of each Ordovician series yielded $K_{max}$ values with different preferred orientations for each of the five target outcrops (Table 5; Fig. 7, Figure S10). The centroid $D\text{-}K_{max}$ values of the Lower Ordovician samples were 169° at LJ, 168° at HH, 170° at JF, 171° at NS and 167° at YH. The centroid $D\text{-}K_{max}$ values of the Middle Ordovician samples were 136° at LJ, 139° at HH, 138° at JF, 140° at NS and 142° at YH. The centroid $D\text{-}K_{max}$ values of the Upper Ordovician samples were 90° at LJ, 89° at HH, 88° at JF, 93° at NS and 95° at YH (modern coordinates; Table 5; Fig. 7, Figure S10).
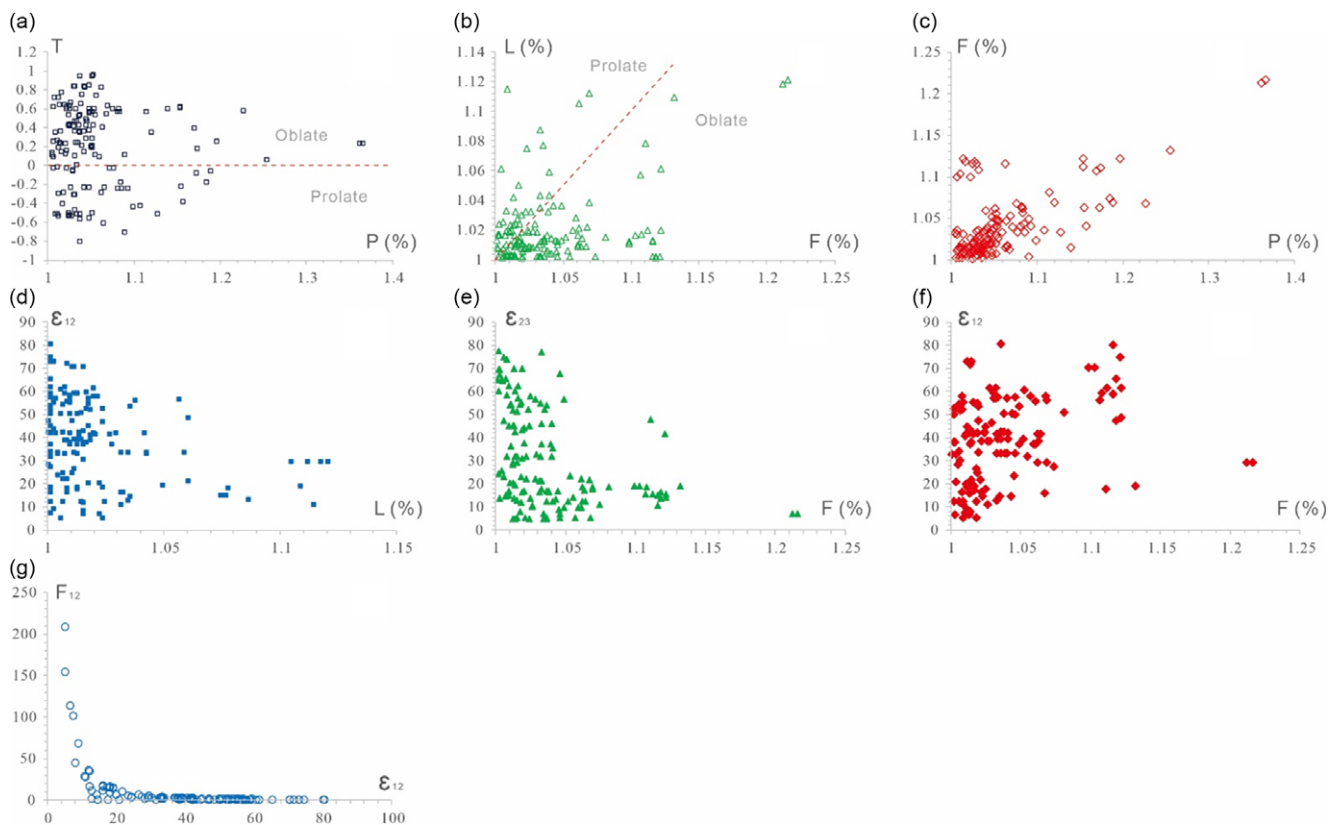
**Fig. 5.** (Colour online) Relationships between the AMS parameters of (a) P and T, (b) F and L, (c) P and F, (d) L and $\epsilon_{12}$, (e) F and $\epsilon_{23}$, (f) F and $\epsilon_{12}$, and (g) $\epsilon_{12}$ and $F_{12}$ for the Ordovician units at the YH outcrop (n = 148). The results for other outcrops (i.e. LJ, FD, YK, YS, YJ, HH, JF and NS) are provided in Figures S2–S8.

## 5. Discussion

### 5.a. Qualitative reconstruction of paleowind directions

Carbonate platform sediments undergo sedimentary differentiation under the action of long-term prevailing winds. Patterns of wind-related facies have been studied in several modern marine systems, among which the best-studied are the those in the Bahamas and Florida Keys (Kindler & Strasser, 2000; Rankey et al. 2006; Rankey & Reeder, 2011). The dominant winds in the Bahamas are the northeasterly trade winds, and coral reefs form on the margins of the northeast-facing windward platform (e.g. eastern side of Andros Island). In contrast, oolitic shoals accumulate on the southwest-facing leeward margins (Principaud et al. 2015; Dravis & Wanless, 2017). Patterns of wind-related facies have also been studied in ancient carbonate platforms. For example, paleowind analysis was conducted on the Cambrian–Ordovician Shanganning Carbonate Platform of the North China Craton (Hu et al. 2020a, 2020b). The study utilized a combination of microfacies analysis and AMS data to evaluate wind-related controls and documented metazoan reefs consisting of corals, stromatoporoids and sponges on the windward platform margin and oolitic grainstones and microbial reefs on the leeward margin (Hu et al. 2020a, 2020b).

The sedimentary differentiation of oolitic and intraclastic grainstones described above qualitatively indicates the general wind direction in the present study (Table 1; Figs. 3, 4). The spatial distribution of specific microfacies and sediment types shows a polarity across the YCP, which helps distinguish between the windward and leeward margins of the platform. Oolitic sands dominate the leeward margins of platforms, and

water in these areas originates from the platform interior and is relatively warm and partially degassed (Principaud et al. 2015; Dravis & Wanless, 2017; Zhang-YY et al. 2017; Hu et al. 2020a, 2020b; Hu et al. 2023a). Therefore, the observed polarity of facies across the YCP is consistent with strong paleowinds, presumably the trade winds, which originate from the northwest (modern coordinates).

### 5.b. Quantitative reconstruction of paleowind directions

AMS can be used to determine the prevailing paleowind directions (Zhang et al. 2010; Nawrocki et al. 2018; Hu et al. 2020a, 2020b; Hu et al. 2022; Hu et al. 2023a). Examples in previous studies include the reconstruction of the route of the paleomonsoon along a west-to-east transect in the Chinese Loess Plateau using AMS (Zhang et al. 2010), and reconstruction of paleowind directions and sources of detrital material archived in the Roxolany loess section, southern Ukraine (Nawrocki et al. 2018). The AMS orientations of the study samples could be explained based on a model of strong unidirectional flow (Fig. S1B; Tarling & Hrouda, 1993; Hu et al. 2020a, 2020b), which demonstrated the greatest agreement with the distribution of data in the current study (Figs. 6, 7). Most grains in this model were oriented parallel to the unidirectional flow (Fig. S1B; Tarling & Hrouda, 1993; Hu et al. 2020a, 2020b). However, paleocurrent directions antipodal to (i.e. 180° away from) the estimated current vectors cannot be excluded given the shallowness of the observed AMS $K_{max}$ inclinations (< 20°; Figs. 6, 7; Hu et al. 2020a, 2020b; Hu et al. 2023a).

Two opposite paleowind directions can be roughly determined based on the AMS results obtained herein. The paleomagnetic

**Table 2.** The robustness of statistical calculations was increased by limiting calculations to Cambrian samples, for which $F_{12} > 4$, $\epsilon_{12} < 22.5°$ and $I\text{-}K_{min} > 70°$. Detailed information is provided in Figs. 6, S9

| Outcrops | Lower Cambrian | Middle Cambrian | Upper Cambrian |
|---|---|---|---|
| LJ | (26/42)62% | (26/48)54% | (35/46)76% |
| FD | (21/49)43% | (29/45)64% | (23/46)50% |
| YK | (27/53)51% | (31/51)61% | (29/45)64% |
| YS | (37/48)77% | (30/43)70% | (24/42)57% |
| YJ | (31/49)63% | (31/45)69% | (20/43)47% |
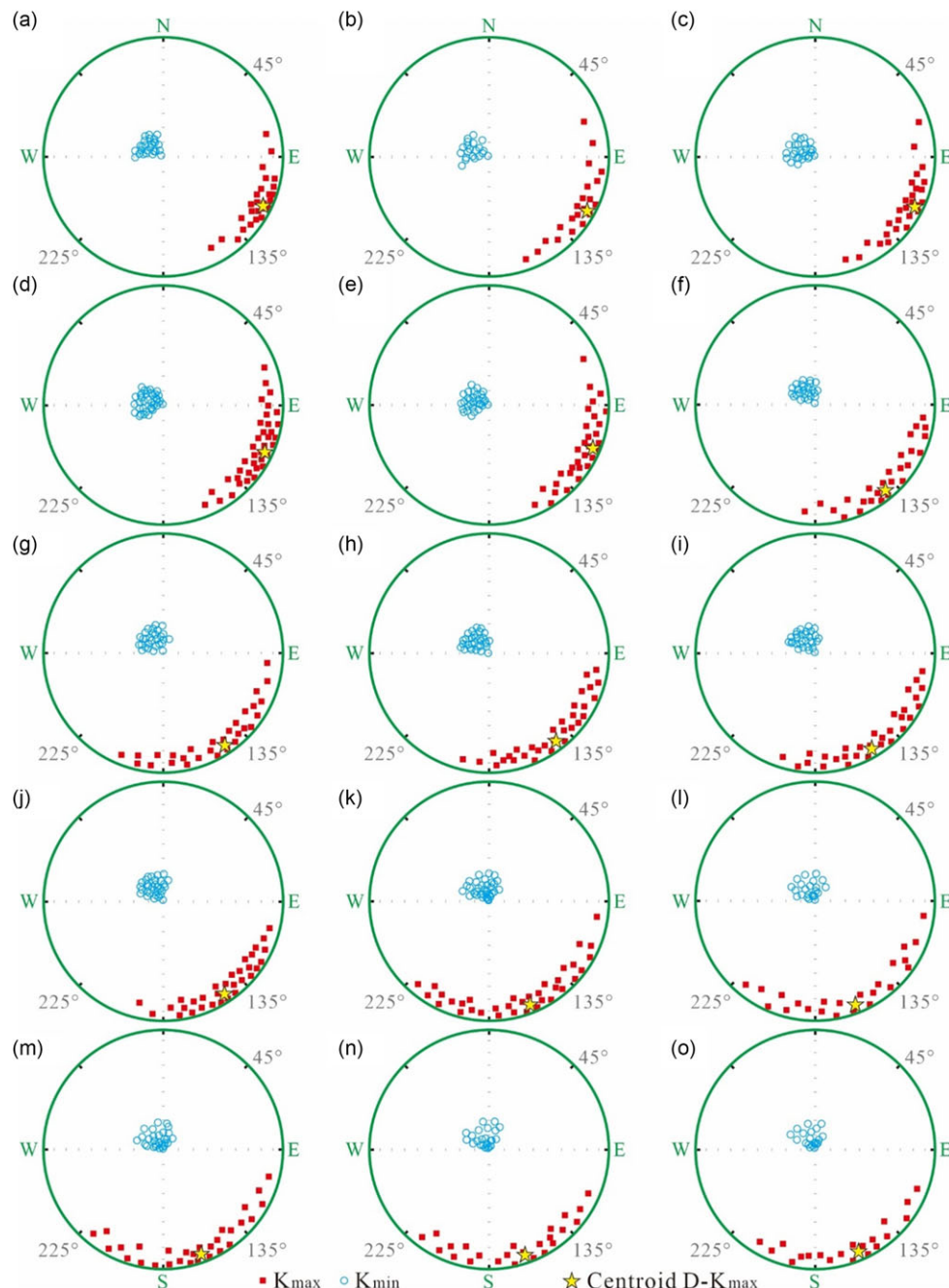


**Fig. 6.** (Colour online) Equal-area projections (modern coordinates) of AMS principal axes of selected samples (according to criteria for which F12 > 4, $\epsilon$12 < 22.5°, and I-K$_{min}$ > 70°) for each Cambrian series from the five outcrops. (a) Lower Cambrian at the LJ outcrop (n = 26). (b) Lower Cambrian at the FD outcrop (n = 21). (c) Lower Cambrian at the YK outcrop (n = 27). (d) Lower Cambrian at the YS outcrop (n = 37). (e) Lower Cambrian at the YJ outcrop (n = 31). (f) Middle Cambrian at the LJ outcrop (n = 26). (g) Middle Cambrian at the FD outcrop (n = 29). (h) Middle Cambrian at the YK outcrop (n = 31). (i) Middle Cambrian at the YS outcrop (n = 30). (j) Middle Cambrian at the YJ outcrop (n = 31). (k) Upper Cambrian at the LJ outcrop (n = 35). (l) Upper Cambrian at the FD outcrop (n = 23). (m) Upper Cambrian at the YK outcrop (n = 29). (n) Upper Cambrian at the YS outcrop (n = 24). (o) Upper Cambrian at the YJ outcrop (n = 20). K$_{max}$ = maximum principal axes of the 3D AMS ellipsoid; K$_{min}$ = minimum principal axes of the 3D AMS ellipsoid; and D-K$_{max}$ = declination of the maximum principal axes of the 3D AMS ellipsoid.

**Table 3.** Maximum AMS axis ($K_{max}$) with different preferred orientations and centroid D-$K_{max}$ values for each of the five study outcrops for each Cambrian series. Detailed information is provided in Fig. 6

| Outcrops | Lower Cambrian | Middle Cambrian | Upper Cambrian |
|---|---|---|---|
| LJ | 78°–152° (centroid 116°) | 98°–186° (centroid 141°) | 98°–221° (centroid 158°) |
| FD | 70°–161° (centroid 119°) | 96°–202° (centroid 146°) | 98°–220° (centroid 159°) |
| YK | 72°–164° (centroid 117°) | 99°–194°(centroid 143°) | 105°–219° (centroid 160°) |
| YS | 69°–157° (centroid 115°) | 100°–197° (centroid 149°) | 114°–218° (centroid 161°) |
| YJ | 64°–156° (centroid 113°) | 104°–194° (centroid 146°) | 111°–212° (centroid 157°) |
| **Mean** | 116° ± 52° | 145° ± 57° | 159° ± 62° |

**Table 4.** The robustness of statistical calculations was increased by limiting calculations to Ordovician samples, for which $F_{12} > 4$, $\epsilon_{12} < 22.5°$ and I-$K_{min} > 70°$. Detailed information is provided in Figs. 7, S10

| Outcrops | Lower Ordovician | Middle Ordovician | Upper Ordovician |
|---|---|---|---|
| LJ | (24/48)50% | (30/43)70% | (24/47)51% |
| HH | (23/51)45% | (36/50)72% | (28/38)74% |
| JF | (22/53)42% | (40/51)78% | (30/40)75% |
| NS | (30/49)61% | (24/45)53% | (31/41)76% |
| YH | (32/55)58% | (23/52)44% | (18/41)44% |

results of the Early, Middle and Late Cambrian were 116° ± 52°, 145° ± 57° and 159° ± 62°, respectively (Table 3; Fig. 6), with paleowind directions of 116° ± 52°, 145° ± 57° and 159° ± 62°, respectively, or 296° ± 52°, 325° ± 57° and 339° ± 62°, respectively (modern coordinates; Fig. 8a–c). The paleomagnetic results of the Early, Middle and Late Ordovician were 169° ± 70°, 139° ± 73° and 91° ± 68°, respectively (Table 5; Fig. 7), with paleowind directions of 169° ± 70°, 139° ± 73° and 91° ± 68°, respectively, or 349° ± 70°, 319° ± 73° and 271° ± 68°, respectively (modern coordinates; Fig. 8d–f). The final quantitative prevailing paleowind directions can be determined by combining information on the sedimentary differentiation (see section 5.a). The paleowind directions of the Early, Middle and Late Cambrian were 296° ± 52°, 325° ± 57° and 339° ± 62°, respectively (modern coordinates; Fig .8a–c). The paleowind directions of the Early, Middle and Late Ordovician were 349° ± 70°, 319° ± 73° and 271° ± 68°, respectively (modern coordinates; Fig. 8d–f).

Marine carbonate platforms are generally located within the trade winds belt at low latitudes (such as The Bahamas, Great Barrier Reef and Shanganning Carbonate Platform). These areas were affected by the prevailing paleowind direction throughout the year, with sedimentary differentiation following a specific trend (Orpin & Ridd, 2012; Puga-Bernabéu *et al.* 2013; Principaud *et al.* 2015; Dravis & Wanless, 2017; Hu *et al.* 2020a, 2020b). Although sedimentary differentiation cannot be used to quantitatively reconstruct the paleowind directions, it can be used to determine the approximate orientation. Although AMS cannot be used to determine the general orientation of paleowind direction, its quantitative ability can compensate for the non-quantification of sedimentary differentiation. The complementary of sedimentary differentiation and AMS allows for the quantitative determination of the prevailing paleowind directions, thereby providing a theoretical basis for the study of Cambrian–Ordovician paleoclimate in this area.

## 5.c. Significance of paleowind directions for paleogeography

The prevailing paleowind direction acted to regulate sedimentary differentiation in the three zones of the YCP, which had important paleogeographic implications. The YCP was located in the low latitudes during the Cambrian–Ordovician (Huang *et al.* 2000; Popov *et al.* 2009; Nardin *et al.* 2011; Torsvik & Cocks, 2013; Cocks & Torsvik, 2021; Harper *et al.* 2021). However, its exact position remains a matter of debate due to the lack of sufficient palaeomagnetic data. The determination of the position of the YCP would refine the current knowledge of the prevailing wind direction by as much as 90°, since trade winds in the Northern Hemisphere blow from northeast to southwest, whereas those in the Southern Hemisphere blow from southeast to northwest (Kajtar *et al.* 2018; Helfer *et al.* 2020, 2021). The present geographic orientation of the Yangtze Block indicates that the prevailing paleowind directions were from the northwest, north and west (Tables 3, 5; Fig. 8). Therefore, the Yangtze Block has rotated after the Ordovician.

The prevailing wind directions of the trade winds belt change slightly for different positions. The prevailing wind direction is nearly south (155°–180°) when positioned far from the Equator in the Southern Hemisphere and nearly east (90°–115°) when near the Equator in the Southern Hemisphere (Kajtar *et al.* 2018; Helfer *et al.* 2020, 2021). The YCP was located at latitudes of ~24°S, ~28°S, ~21°S during the Late Cambrian, Early Ordovician and Middle Ordovician, respectively (Torsvik & Cocks, 2013; Cocks & Torsvik, 2021). The relevant paleowind directions are ~170°, ~177° and ~165°; all directions are approximate values, but all are slightly less than 180° (paleo-coordinates). This study provides evidence for the paleogeography of the YCP during the Cambrian–Ordovician in terms of the prevailing paleowind directions over the YCP and the trade winds in the Northern and Southern hemispheres (southeast wind in the Southern Hemisphere and northeast wind in the Northern Hemisphere). For the Early Cambrian, the samples collected for this study were concentrated in the upper part of the Lower Cambrian, so the measurement results only correspond to the late stage of the Early Cambrian. For the Late Ordovician, the samples collected for this study were concentrated in the lower part of the Upper Ordovician, so the measurement results only correspond to the early stage of the Late Ordovician.

The current position of the YCP would indicate that its paleowind directions were 296° ± 52° during the Early Cambrian, 325° ± 57° during the Middle Cambrian, 339° ± 62° during the Late Cambrian, 349° ± 70° during the Early Ordovician, 319° ± 73° during the Middle Ordovician and 271° ± 68° during the Late Ordovician (Tables 3, 5; Fig. 8). This conclusion is
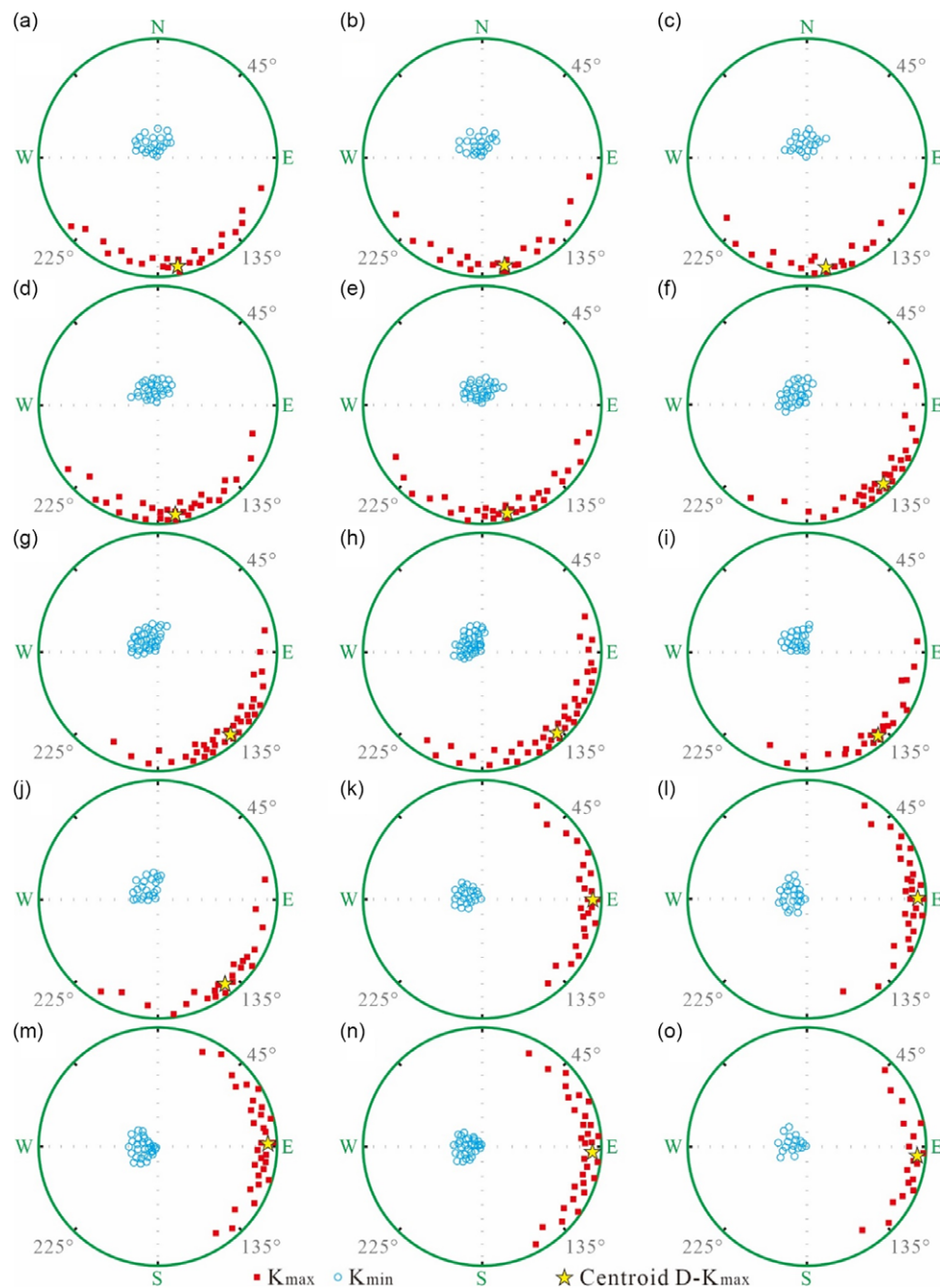
**Fig. 7.** (Colour online) Equal-area projections (modern coordinates) of AMS principal axes of selected samples (according to criteria for which F12 > 4, ε12 < 22.5° and I-K$_{min}$ > 70°) for each Ordovician series from the five outcrops. (a) Lower Ordovician at the LJ outcrop (n = 24). (b) Lower Ordovician at the HH outcrop (n = 23). (c) Lower Ordovician at the JF outcrop (n = 22). (d) Lower Ordovician at the NS outcrop (n = 30). (e) Lower Ordovician at the YH outcrop (n = 32). (f) Middle Ordovician at the LJ outcrop (n = 30). (g) Middle Ordovician at the HH outcrop (n = 36). (h) Middle Ordovician at the JF outcrop (n = 40). (i) Middle Ordovician at the NS outcrop (n = 24). (j) Middle Ordovician at the YH outcrop (n = 23). (k) Upper Ordovician at the LJ outcrop (n = 24). (l) Upper Ordovician at the HH outcrop (n = 28). (m) Upper Ordovician at the JF outcrop (n = 30). (n) Upper Ordovician at the NS outcrop (n = 31). (o) Upper Ordovician at the YH outcrop (n = 18). K$_{max}$ = maximum principal axes of the 3D AMS ellipsoid; K$_{min}$ = minimum principal axes of the 3D AMS ellipsoid; and D-K$_{max}$ = declination of maximum principal axes of the 3D AMS ellipsoid.

consistent with the most recent knowledge of paleogeography (e.g. Torsvik & Cocks, 2013; Cocks & Torsvik, 2021): (1) the YCP was located in the Southern Hemisphere (~14°S), and the prevailing paleowind direction was ~133° (paleo-coordinates) during the Early Cambrian. The plate has rotated ~197° counterclockwise since the Early Cambrian, so the paleowind direction was ~296° in modern coordinates; (2) the YCP was located at ~18°S, and the prevailing paleowind direction was ~156° (paleo-coordinates)

during the Middle Cambrian. The plate has rotated ~191° counterclockwise since the Middle Cambrian, so the paleowind direction was ~325° in modern coordinates; (3) the YCP was located at ~24°S and the prevailing paleowind direction was ~168° (paleo-coordinates) during the Late Cambrian. The plate has rotated ~189° counterclockwise since the Late Cambrian, so the paleowind direction was ~339° in modern coordinates; (4) the YCP was located at ~28°S and the prevailing paleowind direction was ~173°

**Table 5.** Maximum AMS axis ($K_{max}$) with different preferred orientations and centroid D-$K_{max}$ values for each of the five study outcrops for each Ordovician series. Detailed information is provided in Fig. 7

| Outcrops | Lower Ordovician | Middle Ordovician | Upper Ordovician |
|---|---|---|---|
| LJ | 107°–232° (centroid 169°) | 67°–211° (centroid 136°) | 31°–142° (centroid 90°) |
| HH | 100°–237° (centroid 168°) | 79°–203° (centroid 139°) | 32°–159° (centroid 89°) |
| JF | 105°–234° (centroid 170°) | 71°–212° (centroid 138°) | 25°–146° (centroid 88°) |
| NS | 107°–235° (centroid 171°) | 84°–202° (centroid 140°) | 27°–151° (centroid 93°) |
| YH | 105°–239° (centroid 167°) | 80°–211° (centroid 142°) | 45°–146° (centroid 95°) |
| **Mean** | 169° ± 70° | 139° ± 73° | 91° ± 68° |
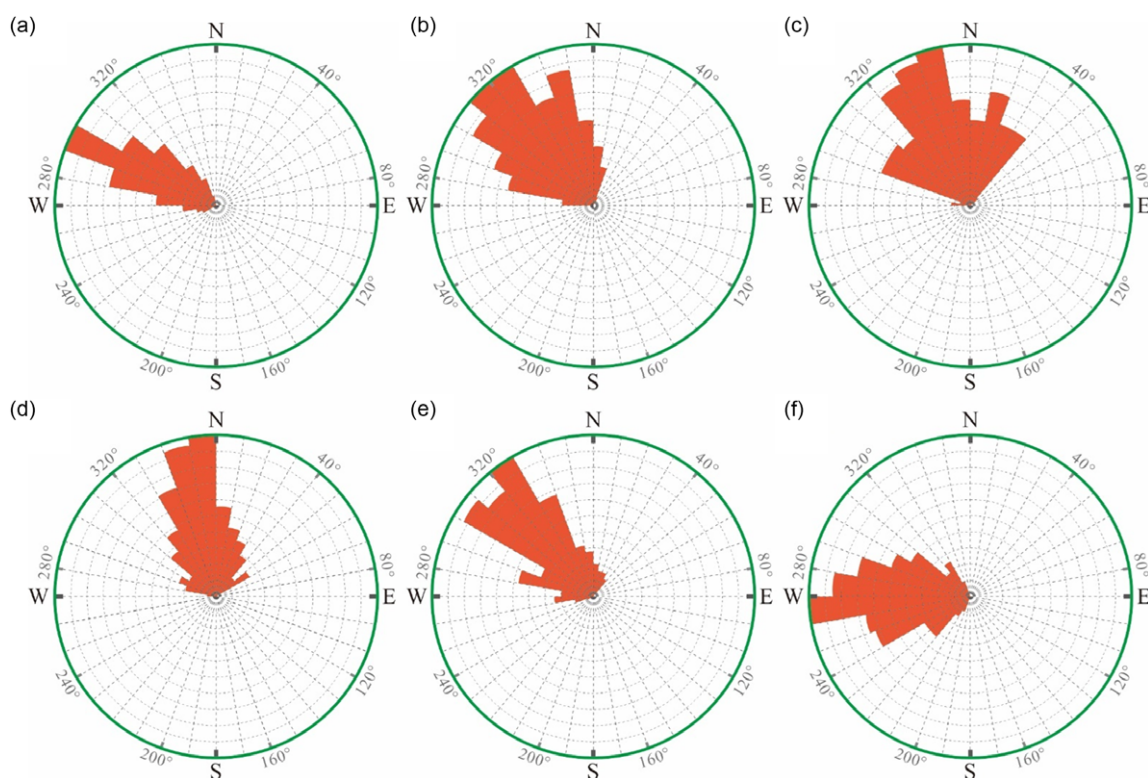


**Fig. 8.** (Colour online) Comprehensively interpretative rose diagram showing the prevailing paleowind directions for each epoch of the Cambrian–Ordovician. (a) Early Cambrian. (b) Middle Cambrian. (c) Late Cambrian. (d) Early Ordovician. (e) Middle Ordovician. (f) Late Ordovician.

(paleo-coordinates) during the Early Ordovician. The plate has rotated ~184° counterclockwise since the Early Ordovician, so the paleowind direction was ~349° in modern coordinates; (5) the YCP was located at ~21°S, and the prevailing paleowind direction was ~165° (paleo-coordinates) during the Middle Ordovician. The plate has rotated ~206° counterclockwise since the Middle Ordovician, so the paleowind direction was ~319° in modern coordinates; and (6) the YCP was located at ~16°S and the prevailing paleowind direction was ~136° (paleo-coordinates) during the Late Ordovician. The plate has rotated ~225° counterclockwise since the Late Ordovician, so the paleowind direction was ~271° in modern coordinates (Torsvik & Cocks, 2013; Cocks & Torsvik, 2021; Fig. 9).

The determination of paleowind directions can be of geological significance for ancient carbonate platforms or basins. For example, as shown in the present study, the paleogeography of a plate can be constrained using wind directions.

## 6. Conclusions

The YCP was located in the low-latitude trade winds belt during the Cambrian–Ordovician and was affected by the prevailing wind directions. Analysis of the sedimentary differentiation of carbonate microfacies and AMS on the platform indicated that the paleowind directions over the YCP during the Early, Middle and Late Cambrian were 296° ± 52°, 325° ± 57° and 339° ± 62° respectively, whereas those during the Early, Middle and Late Ordovician were 349° ± 70°, 319° ± 73° and 271° ± 68°, respectively (modern coordinates). The present study quantitatively reconstructed the prevailing paleowind directions over the YCP through an analysis of sedimentary differentiation and AMS. The results of the present study can provide a reference for the study of the paleoclimate of the YCP.

The present study provided evidence for the location of the YCP during the Cambrian–Ordovician through the corresponding relationship between the prevailing paleowind directions over the YCP and the trade winds in the Northern and Southern hemispheres.
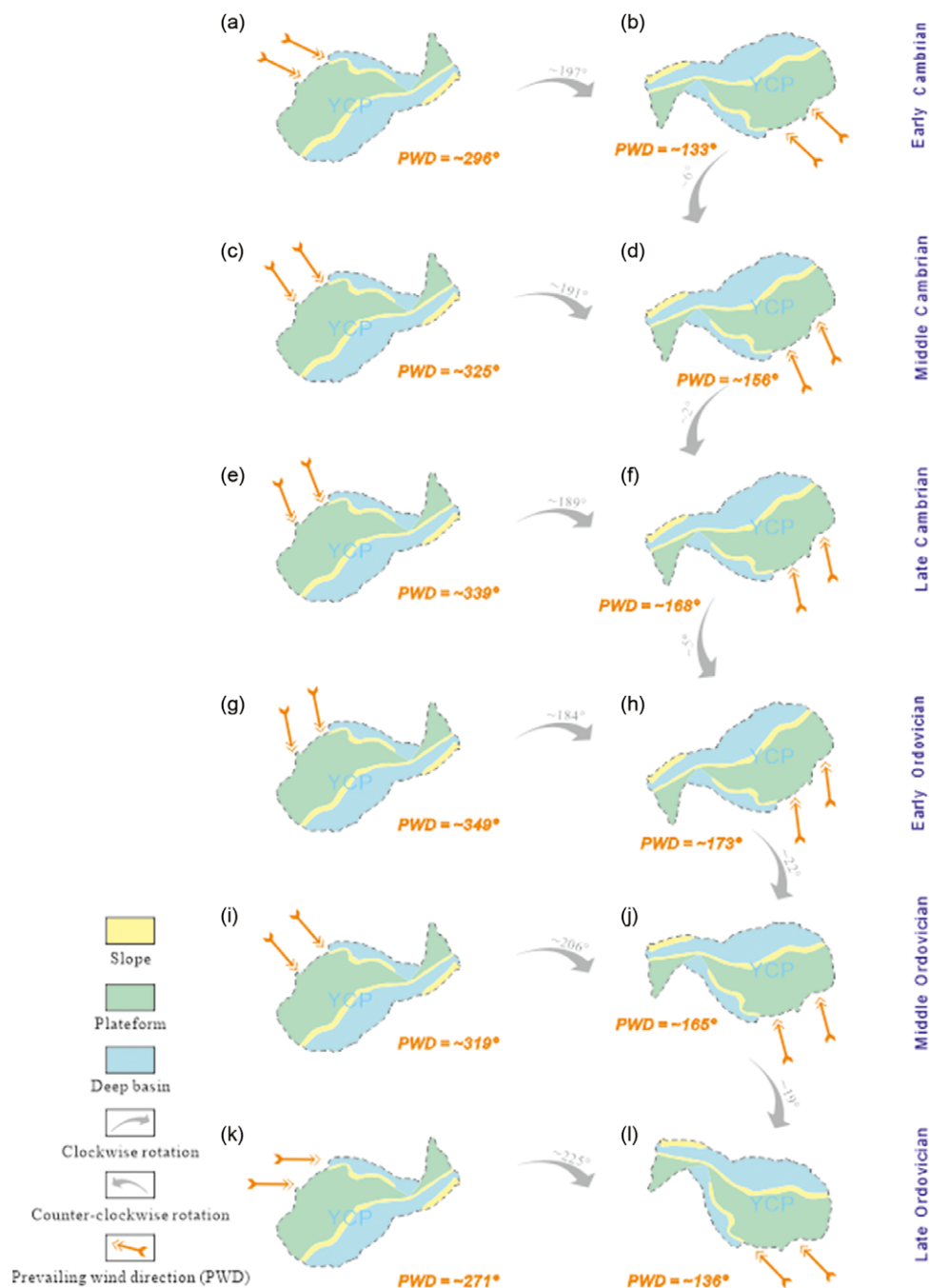
**Fig. 9.** (Colour online) Relationship between present and Cambrian-Ordovician geographic orientations of the YCP. Paleowind orientations of the YCP are shown in modern coordinate (left) and paleo-coordinate (right) frameworks. Data are for Early Cambrian (a, b), Middle Cambrian (c, d), Late Cambrian (e, f), Early Ordovician (g, h), Middle Ordovician (i, j) and Late Ordovician (k, l). The prevailing wind directions for each Cambrian-Ordovician series are based on the AMS results from Tables 3 and 5 as well as Figs. 6, 7. Syn-and post-Cambrian and Ordovician tectonic rotations are shown by tapered grey arrows.

The YCP was located at ~14°S, ~18°S and ~24°S during the Early, Middle and Late Cambrian, respectively; corresponding values for the Early, Middle and Late Ordovician were ~28°S, ~21°S and ~16° S, respectively. The results of the present study can provide a reference for the study of the paleogeography of the YCP.

**Supplementary material.** To view supplementary material for this article, please visit https://doi.org/10.1017/S0016756823000286

**Data availability.** All relevant data used for the research described in this article are included in the article and/or its supplementary files. Upon the request to the corresponding author (majinghui10@163.com) or first author (huchenlin@tom.com), the data are available.

## References

**Aria C and Caron JB** (2019) A middle Cambrian arthropod with chelicerae and proto-book gills. *Nature* **573**, 586–89. doi: 10.1038/s41586-019-1525-4.

**Chang HJ, Chu XL, Feng LJ, Huang J and Chen YL** (2018) Marine redox stratification on the earliest Cambrian (ca. 542–529 Ma) Yangtze Platform. *Palaeogeography, Palaeoclimatology, Palaeoecology* **504**, 75–85. doi: 10.1016/j.palaeo.2018.05.007.

**Che ZQ, Tan XC, Deng JT and Jin MD** (2019) The characteristics and controlling factors of facies-controlled coastal eogenetic karst: insights from the fourth member of Neoproterozoic Dengying formation, Central Sichuan Basin, China. *Carbonates and Evaporites* **34**, 1771–83. doi: 10.1007/s13146-019-00524-0.

**Chen X, Rong JY, Li Y and Boucot AJ** (2004) Facies patterns and geography of the Yangtze region, South China, though the Ordovician and Silurian transition. *Palaeogeography, Palaeoclimatology, Palaeoecology* **204**, 353–72. doi: 10.1016/S0031-0182(03)00736-3.

**Cheng SH, Li B, Zhang K, Liu WW, Peng J, Hou MC, Wen M, Xia QS, Wang X, Liu XX, Zhong L, Huang YZ, Liu YY, Yuan MH and Yao Y** (2020) Study on the mechanism of organic matter enrichment in early Cambrian marine shales in the lower Yangtze area, South China: an example using well jxy1. *Geofluids* **2020**. doi: 10.1155/2020/2460302.

**Cheng XY, Ding WL, Pan L, Zou YT, Li YT, Yin YX and Ding SH** (2022) Geometry and kinematics characteristics of strike-slip fault zone in complex structure area: a case study from the South No. 15 strike-slip fault zone in the Eastern Sichuan Basin, China. *Frontiers in Earth Science* **10**, 922664. doi: 10.3389/feart.2022.922664.

**Cocks LRM and Torsvik TH** (2021) Ordovician palaeogeography and climate change. *Gondwana Research* **100**, 53–72. doi: 10.1016/j.gr.2020.09.008.

**Constable C and Tauxe L** (1990) The bootstrap for magnetic susceptibility tensors. *Journal of Geophysical Research: Solid Earth* **95**, 8383–95. doi: 10.1029/JB095iB06p08383.

**Dalziel IW** (2014) Cambrian transgression and radiation linked to an Iapetus-Pacific oceanic connection? *Geology* **42**, 979–82. doi: 10.1130/G35886.1.

**Dong L, Han CC, Santosh M, Qiu YK, Liu G, Ma JH, He H and Hu CL** (2022) Factors influencing the pore structure and gas-bearing characteristics of Shales: insights from the Longmaxi formation, Southern Sichuan Basin and Northern Yunnan-Guizhou Depression, China. *Geofluids*. doi: 10.1155/2022/1692516.

**Dravis JJ and Wanless HR** (2017) Impact of strong easterly trade winds on carbonate petroleum exploration-relationships developed from Caicos Platform, southeastern Bahamas. *Marine and Petroleum Geology* **85**, 272–300. doi: 10.1016/j.marpetgeo.2017.04.010.

**Fang X, Li WJ, Zhang JP, Song YY and Zhang YD** (2020) Paleo-environmental changes during the Middle–Late Ordovician transition on the Yangtze Platform, South China and their ecological implications. *Palaeogeography, Palaeoclimatology, Palaeoecology* **560**, 109991. doi: 10.1016/j.palaeo.2020.109991.

**Flügel E** (2013) *Classification——A Name for Your Sample, Chapter 8 in Microfacies of Carbonate Rocks: Analysis, Interpretation and Application*: Springer Science & Business Media, pp. 339–64. doi: 10.1007/978-3-662-08726-8.

**Fu QL, Hu SY, Xu ZH, Zhao WZ, Shi SY and Zeng HL** (2020) Depositional and diagenetic controls on deeply buried Cambrian carbonate reservoirs: Longwangmiao formation in the Moxi–Gaoshiti area, Sichuan Basin, southwestern China. *Marine and Petroleum Geology* **117**, 104318. doi: 10.1016/j.marpetgeo.2020.104318.

**Gao P, Li SJ, Lash GG, Yan DT, Zhou Q and Xiao XM** (2021) Stratigraphic framework, redox history, and organic matter accumulation of an Early Cambrian intraplatfrom basin on the Yangtze Platform, South China. *Marine and Petroleum Geology* **130**, 105095. doi: 10.1016/j.marpetgeo.2021.105095.

**Ge XY, Mou CL, Yu Q, Liu W, Men X and He JL** (2019) The geochemistry of the sedimentary rocks from the Huadi No. 1 well in the Wufeng-Longmaxi formations (Upper Ordovician-Lower Silurian), South China, with implications for paleoweathering, provenance, tectonic setting and paleoclimate. *Marine and Petroleum Geology* **103**, 646–60. doi: 10.1016/j.marpetgeo.2018.12.040.

**Gong HJ, Zhang R, Yue LP, Zhang YX and Li JX** (2015) Magnetic fabric from Red clay sediments in the Chinese Loess Plateau. *Scientific Reports* **5**, 1–6. doi: 10.1038/srep09706.

**Gu ZD, Lonergan L, Zhai XF, Zhang BM and Lu WH** (2021) The formation of the Sichuan Basin, South China, during the Late Ediacaran to Early Cambrian. *Basin Research* **33**, 2328–57. doi: 10.1111/bre.12559.

**Gu ZD, Yin JF, Yuan M, Bo DM, Liang DX, Zhang H and Zhang L** (2015) Accumulation conditions and exploration directions of natural gas in deep subsalt Sinian-Cambrian System in the eastern Sichuan Basin, SW China. *Petroleum Exploration and Development* **42**, 152–66. doi: 10.1016/S1876-3804(15)30002-1.

**Han CC, Tian JJ, Hu CL, Liu HL, Wang WF, Huan ZP and Feng S** (2020) Lithofacies characteristics and their controlling effects on reservoirs in buried hills of metamorphic rocks: a case study of late Paleozoic units in the Aryskum depression, South Turgay Basin, Kazakhstan. *Journal of Petroleum Science and Engineering* **191**, 107–37. doi: 10.1016/j.petrol.2020.107137.

**Harper DA, Cascales-Miñana B, Kroeck DM and Servais T** (2021) The palaeogeographical impact on the biodiversity of marine faunas during the Ordovician radiations. *Global and Planetary Change* **207**, 103665. doi: 10.1016/j.gloplacha.2021.103665.

**He L, Wang YP and Chen DF** (2019) Geochemical features of sedimentary environment and paleoclimate during Late Ordovician to Early Silurian in southern Sichuan Basin. *Geochimica* **48**, 555–66. doi: 10.19700/j.0379-1726.2019.06.004.

**Helfer KC, Nuijens L, De Roode SR and Siebesma AP** (2020) How wind shear affects trade-wind cumulus convection. *Journal of Advances in Modeling Earth Systems* **12**, e2020MS002183. doi: 10.1029/2020MS002183.

**Helfer KC, Nuijens L and Dixit VV** (2021) The role of shallow convection in the momentum budget of the trades from large-eddy-simulation hindcasts. *Quarterly Journal of the Royal Meteorological Society* **147**, 2490–505. doi: 10.1002/qj.4035.

**Hoyal Cuthill JF, Guttenberg N and Budd GE** (2020) Impacts of speciation and extinction measured by an evolutionary decay clock. *Nature* **588**, 636–41. doi: 10.1038/s41586-020-3003-4.

**Hu CL, Han CC, Ma JH, Deng L and Zhao LF** (2022) Paleowind directions over the Tarim Block during the Mesoproterozoic, Northwestern China. *Minerals* **12**, 1435. doi: 10.3390/min12111435.

**Hu CL, Han CC, Ma JH, Wang WF, Zhao FY and Sun WX** (2023a) Reconstruction of paleowind directions during the Cambrian-Ordovician in the Tarim Basin, Northwestern China. *Palaeogeography, Palaeoclimatology, Palaeoecology* **609**, 111316. doi: 10.1016/J.PALAEO.2022.111316.

**Hu CL, Han CC, Tian JJ, Fu ZQ, Ma JH and Algeo TJ** (2023b) Lithofacies and diagenetic controls on tight silty and sandy Upper Triassic reservoirs of the Heshui Oil Field (Ordos Basin, North China). *SPE Reservoir Evaluation & Engineering* **26**, 19–37. doi: 10.2118/214289-PA.

**Hu CL, Zhang YF, Feng DY, Wang M, Jiang ZX and Jiao CW** (2017) Flume tank simulation on depositional mechanism and controlling factors of beach-bar reservoirs. *Journal of Earth Science* **28**, 1153–62. doi: 10.1007/s12583-016-0929-4.

**Hu CL, Zhang YF, Jiang ZX, Wang M and Han C** (2021) Development of large-scale sand bodies in a fault-bounded lake basin: Pleistocene-Holocene Poyang Lake, Southern China. *Journal of Paleolimnology* **65**, 407–28. doi: 10.1007/s10933-021-00179-9.

**Hu CL, Zhang YF, Jiang ZX, Wang M, Han C and Algeo TJ** (2020a) Tectonic and paleogeographic controls on development of the Early–Middle Ordovician Shanganning carbonate platform, Ordos Basin, North China. *AAPG Bulletin* **104**, 565–93. doi: 10.1306/06121918175.

**Hu CL, Zhang YF, Tian JJ, Wang WF, Han CC, Wang HC, Li X, Feng S, Han C and Algeo TJ** (2020b) Influence of paleo-Trade Winds on facies patterns of the Cambrian Shanganning carbonate platform, North China.

*Palaeogeography, Palaeoclimatology, Palaeoecology* **552**, 109556. doi: 10.1016/j.palaeo.2019.109556.

**Huang BC, Zhu RX, Otofuji Y and Yang ZY** (2000) The early Paleozoic paleogeography of the North China block and the other major blocks of China. *Chinese Science Bulletin* **45**, 1057–8. doi: 10.1007/BF02887174.

**Huang HY, He DF, Li D, Li YQ, Zhang WK and Chen JJ** (2020) Geochemical characteristics of organic-rich shale, Upper Yangtze Basin: implications for the Late Ordovician–Early Silurian orogeny in South China. *Palaeogeography, Palaeoclimatology, Palaeoecology* **554**, 109822. doi: 10.1016/j.palaeo.2020.109822.

**Jelinek V** (1981) Characterization of the magnetic fabric of rocks. *Tectonophysics* **79**, T63–7. doi: 10.1016/0040-1951(81)90110-4.

**Jin CS, Li C, Algeo TJ, Planavsky NJ, Cui H, Yang XL, Zhao YL, Zhang XL and Xie SS** (2016) A highly redox-heterogeneous ocean in South China during the early Cambrian (~ 529–514 Ma): implications for biota-environment co-evolution. *Earth and Planetary Science Letters* **441**, 38–51. doi: 10.1016/j.epsl.2016.02.019.

**Jin MD, Li BS, Zhu X, Dai LC, Jiang ZL, Wu H, Li H and Yang PY** (2020) Characteristics and main controlling factors of reservoirs in the fourth member of Sinian Dengying formation in Yuanba and its peripheral area, northeastern Sichuan Basin, SW China. *Petroleum Exploration and Development* **47**, 1172–82. doi: 10.1016/S1876-3804(20)60127-1.

**Kajtar JB, Santoso A, McGregor S, England MH and Baillie Z** (2018) Model under-representation of decadal Pacific trade wind trends and its link to tropical Atlantic bias. *Climate Dynamics* **50**, 1471–84. doi: 10.1007/s00382-017-3699-5.

**Karlstrom K, Hagadorn J, Gehrels G, Matthews W, Schmitz M, Madronich L, Mulder J, Pecha M, Giesler D and Crossey L** (2018) Cambrian Sauk transgression in the Grand Canyon region redefined by detrital zircons. *Nature Geoscience* **11**, 438–43. doi: 10.1038/s41561-018-0131-7.

**Kindler P and Strasser A** (2000) Palaeoclimatic significance of co-occurring wind-and water-induced sedimentary structures in the last-interglacial coastal deposits from Bermuda and the Bahamas. *Sedimentary Geology* **131**, 1–7. doi: 10.1016/S0037-0738(99)00123-2.

**Kröger B** (2018) Changes in the latitudinal diversity gradient during the Great Ordovician Biodiversification event. *Geology* **46**, 127–30. doi: 10.1130/G39587.1.

**Lagroix F and Banerjee SK** (2002) Paleowind directions from the magnetic fabric of loess profiles in central Alaska. *Earth and Planetary Science Letters* **195**, 99–112. doi: 10.1016/S0012-821X(01)00564-7.

**Lagroix F and Banerjee SK** (2004) The regional and temporal significance of primary Aeolian magnetic fabrics preserved in Alaskan loess. *Earth and Planetary Science Letters* **225**, 379–95. doi: 10.1016/j.epsl.2004.07.003.3.

**Lee JH and Riding R** (2018) Marine oxygenation, lithistid sponges, and the early history of Paleozoic skeletal reefs. *Earth-Science Reviews* **181**, 98–121. doi: 10.1016/j.earscirev.2018.04.003.

**Li G, Li ZQ, Li D, Liu HL, Su GP and Yan S** (2022) Basement fault control on the extensional process of a basin: a case study from the Cambrian–Silurian of the Sichuan Basin, South-west China. *Geological Journal*. doi: 10.1002/gj.4492.

**Li L, Tan XC, Zhao LZ, Liu H, Xia JW and Luo B** (2013) Prediction of thin shoal-facies reservoirs in the carbonate platform interior: a case from the Cambrian Xixiangchi Group of the Weiyuan area, Sichuan Basin. *Petroleum Exploration and Development* **40**, 359–66. doi: 10.1016/S1876-3804(13)60043-9.

**Li QJ, Li Y, Wang JP and Kiessling W** (2015) Early Ordovician lithistid sponge–Calathium reefs on the Yangtze Platform and their paleoceanographic implications. *Palaeogeography, Palaeoclimatology, Palaeoecology* **425**, 84–96. doi: 10.1016/j.palaeo.2015.02.034.

**Li W, Fan R, Jia P, Lu YZ, Zhang ZJ, Li X and Deng SH** (2019) Sequence stratigraphy and lithofacies paleogeography of the Middle–Upper Cambrian Xixiangchi Group in the Sichuan Basin and its adjacent area, SW China. *Petroleum Exploration and Development* **46**, 238–52. doi: 10.1016/S1876-3804(19)60005-4.

**Li W, Yu HQ and Deng HB** (2012) Stratigraphic division and correlation and sedimentary characteristics of the Cambrian in central-southern Sichuan Basin. *Petroleum Exploration and Development* **39**, 725–35. doi: 10.1016/S1876-3804(12)60097-4.

**Li YD, Chen YL, Yan W, Dai RX, Xi C and He Y** (2021) Research on sedimentary evolution characteristics of Cambrian Canglangpu formation, Sichuan Basin. *Natural Gas Geoscience* **32**, 1334–46 (in Chinese with English abstract).

**Li YQ, He DF, Li D, Li SJ, Wo YJ, Li CX and Huang HY** (2020) Ediacaran (Sinian) palaeogeographic reconstruction of the Upper Yangtze area, China, and its tectonic implications. *International Geology Review* **62**, 1485–509. doi: 10.1080/00206814.2019.1655670.

**Liang C, Jiang ZX, Yang YT and Wei XJ** (2012) Shale lithofacies and reservoir space of theg Wufeng–Longmaxi formation, Sichuan Basin, China. *Petroleum Exploration and Development* **39**, 736–43. doi: 10.1016/S1876-3804(12)60098-6.

**Liu H, Tan XC, Li YH, Cao J and Luo B** (2018) Occurrence and conceptual sedimentary model of Cambrian gypsum-bearing evaporites in the Sichuan Basin, SW China. *Geoscience Frontiers* **9**, 1179–91. doi: 10.1016/j.gsf.2017.06.006.

**Liu JL, Liu KY, Li CW and Liu WJ** (2020) Tectono-sedimentary evolution of the Late Ediacaran to early Cambrian trough in central Sichuan Basin, China: New insights from 3D stratigraphic forward modelling. *Precambrian Research* **350**, 105826. doi: 10.1016/j.precamres.2020.105826.

**Liu SG, Deng B, Jansa L, Zhong Y, Sun W, Song JM, Wang GZ, Wu J, Li ZW and Tian YH** (2017) The early cambrian mianyang-changning intracratonic sag and its control on petroleum accumulation in the Sichuan Basin, China. *Geofluids* **2017**. doi: 10.1155/2017/6740892.

**Liu SG, Yang Y, Deng B, Zhong Y, Wen L, Sun W, Li ZW, Jansa L, Li JX, Song JM, Zhang XH and Peng HL** (2021) Tectonic evolution of the sichuan basin, southwest China. *Earth-Science Reviews* **213**, 103470. doi: 10.1016/j.earscirev.2020.103470.

**Lu B, Qiu Z, Zhang BH, Li J and Tao HF** (2021) Geological significance of rare earth elements in marine shale during the Late Ordovician–Early Silurian in Sichuan Basin, South China. *Geological Journal* **56**, 1821–40. doi: 10.1002/gj.4027.

**Luo Z, Shao HM, Yan YX, Wang RH, Wang P, Yang Z, Wang YK, Song BR, Cui JG, Wang LY and Man L** (2016) *Rock Thin-Section Identification Standard of SY/T 5368-2016*. China: National Energy Administration, pp. 43 (In Chinese).

**Men X, Mou CL, Ge XY and Wang YC** (2020) Geochemical characteristics of siliceous rocks of Wufeng Formation in the Late Ordovician, South China: assessing provenance, depositional environment, and formation model. *Geological Journal* **55**, 2930–50. doi: 10.1002/gj.3553.

**Miao ZS, Pei YW, Su N, Sheng SZ, Feng B, Jiang H, Liang H and Hong HT** (2022) Spatial and temporal evolution of the Sinian and its implications on petroleum exploration in the Sichuan Basin, China. *Journal of Petroleum Science and Engineering* **210**, 110036. doi: 10.1016/j.petrol.2021.110036.

**Nardin E, Goddéris Y, Donnadieu Y, Hir GL, Blakey RC, Pucéat E and Aretz M** (2011) Modeling the early Paleozoic long-term climatic trend. *Bulletin* **123**, 1181–92. doi: 10.1130/B30364.1.

**Nawrocki J, Gozhik P, Lanczont M, Panczyk M, Komar M, Bogucki A, Williams IS and Czupyt Z** (2018) Palaeowind directions and sources of detrital material archived in the Roxolany loess section (southern Ukraine). *Palaeogeography, Palaeoclimatology, Palaeoecology* **496**, 121–35. doi: 10.1016/j.paleo.2018.01.028.

**Orpin AR and Ridd PV** (2012) Exposure of inshore corals to suspended sediments due to wave-resuspension and river plumes in the central Great Barrier Reef: a reappraisal. *Continental Shelf Research* **47**, 55–67. doi: 10.1016/j.csr.2012.06.013.

**Peters SE and Gaines RR** (2012) Formation of the 'Great Unconformity' as a trigger for the Cambrian explosion. *Nature* **484**, 363–6. doi: 10.1038/nature10969.

**Popov LE, Bassett MG, Zhemchuzhnikov VG, Holmer LE and Klishevich IA** (2009) Gondwanan faunal signatures from early Palaeozoic terranes of Kazakhstan and Central Asia: evidence and tectonic implications. *Geological Society, London, Special Publications* **325**, 23–64. doi: 10.1144/SP325.3.

**Principaud M, Mulder T, Gillet H and Borgomano J** (2015) Large-scale carbonate submarine mass-wasting along the northwestern slope of the Great Bahama Bank (Bahamas): morphology, architecture, and mechanisms. *Sedimentary Geology* **317**, 27–42. doi: 10.1016/j.sedgeo.2014.10.008.

**Puga-Bernabéu A, Webster JM, Beaman RJ and Guilbaud V** (2013) Variation in canyon morphology on the Great Barrier Reef margin, north-eastern Australia: the influence of slope and barrier reefs. *Geomorphology* **191**, 35–50. doi: 10.1016/j.geomorph.2013.03.001.

**Rankey EC and Reeder SL** (2011) Holocene oolitic marine sand complexes of the Bahamas. *Journal of Sedimentary Research* **81**, 97–117. doi: 10.2110/jsr.2011.10.

**Rankey EC, Riegl B and Steffen K** (2006) Form, function and feedbacks in a tidally dominated ooid shoal, Bahamas. *Sedimentology* **53**, 1191–210. doi: 10.1111/j.1365-3091.2006.00807.x.

**Rees AI and Woodall WA** (1975) The magnetic fabric of some laboratory-deposited sediments. *Earth and Planetary Science Letters* **25**, 121–30. doi: 10.1016/0012-821x(75)90188-0.

**Ren Y, Zhong DK, Gao CL, Sun HT, Peng H, Zheng XW and Qiu C** (2019) Origin of dolomite of the lower Cambrian Longwangmiao Formation, eastern Sichuan Basin, China. *Carbonates and Evaporites* **34**, 471–90. doi: 10.1007/s13146-017-0409-7.

**Shi CH, Cao J, Selby D, Tan XC, Luo B and Hu WX** (2020) Hydrocarbon evolution of the over-mature Sinian Dengying reservoir of the Neoproterozoic Sichuan Basin, China: insights from Re–Os geochronology. *Marine and Petroleum Geology* **122**, 104726. doi: 10.1016/j.marpetgeo.2020.104726.

**Stigall AL, Edwards CT, Freeman RL and Rasmussen CM** (2019) Coordinated biotic and abiotic change during the Great Ordovician Biodiversification event: Darriwilian assembly of early Paleozoic building blocks. *Palaeogeography, Palaeoclimatology, Palaeoecology* **530**, 249–70. doi: 10.1016/j.palaeo.2019.05.034.

**Tan Q, Shi ZJ, Tian YM, Wang Y and Wang CC** (2018) Origin of ooids in ooidal-muddy laminites: a case study of the lower Cambrian Qingxudong Formation in the Sichuan Basin, South China. *Geological Journal* **53**, 1716–27. doi: 10.1002/gj.2995.

**Tang YN, Hu CL, Dan SH, Han CC and Liu ZM** (2022) Depositional model for the early Triassic Braided River Delta and controls on oil reservoirs in the Eastern Junggar Basin, Northwestern China. *Minerals* **12**, 1409. doi: 10.3390/min12111409.

**Tarling DH and Hrouda F** (1993) *The Magnetic Anisotropy of Rocks*. London: Chapman and Hall, pp. 220.

**Torsvik TH and Cocks LRM** (2013) New global palaeogeographical reconstructions for the Lower Palaeozoic and their generation. In *Early Palaeozoic Biogeography and Geography* (eds DAT Harper and T Servais, **38**, pp. 5–24. Geological Society of London, Memoir. doi: 10.1144/M38.2.

**Tucker ME and Wright VP** (2009) *Carbonate Sedimentology*. New York: John Wiley & Sons, 481 pp.

**Wang FY, Guan J, Feng WP and Bao LY** (2013) Evolution of overmature marine shale porosity and implication to the free gas volume. *Petroleum Exploration and Development* **40**, 819–24. doi: 10.1016/S1876-3804(13)60111-1.

**Wang Q, Wang XZ and Zeng XY** (2022) Research on reservoir characteristics and main controlling factors of Longwangmiao formation of Cambrian in Sichuan Basin. *Frontiers in Earth Science* **503**. doi: 10.3389/feart.2022.885637.

**Wang Y, Wang SY, Yan HJ, Zhang YJ, Li JZ and Ma DB** (2021) Microbial carbonate sequence architecture and depositional environments of Member IV of the Late Ediacaran Dengying Formation, Gaoshiti–Moxi area, Sichuan Basin, Southwest China. *Geological Journal* **56**, 3992–4015. doi: 10.1002/gj.4146.

**Wang YM, Dong DZ, Huang JL, Li XJ and Wang SF** (2016) Guanyinqiao Member lithofacies of the Upper Ordovician Wufeng formation around the Sichuan Basin and the significance to shale gas plays, SW China. *Petroleum Exploration and Development* **43**, 45–53. doi: 10.1016/S1876-3804(16)30005-2.

**Wang YM, Li XJ, Wang H, Jiang S, Chen B, Ma J and Dai B** (2019) Developmental characteristics and geological significance of the bentonite in the Upper Ordovician Wufeng–Lower Silurian Longmaxi formation in eastern Sichuan Basin, SW China. *Petroleum Exploration and Development* **46**, 687–700. doi: 10.1016/S1876-3804(19)60226-0.

**Wang ZC, Jiang H, Wang TS, Lu WH, Gu ZD, Xu AN, Yang Y and Xu ZH** (2014) Paleo-geomorphology formed during Tongwan tectonization in Sichuan Basin and its significance for hydrocarbon accumulation. *Petroleum Exploration and Development* **41**, 338–45. doi: 10.1016/S1876-3804(14)60038-0.

**Wilson JL, Tucker ME, Crevello PD, Sarg JR and Read JF** (1990) Basement structural controls on Mesozoic carbonate facies in northeastern Mexico——a review. In *Carbonate Platforms: Facies, Sequences and Evolution* (ed ME Tucker), pp. 235–56. New York: John Wiley & Sons.

**Wood R, Liu AG, Bowyer F, Wilby PR, Dunn FS, Kenchington CG, Hoyal Cuthill JF, Mitchell EG and Penny A** (2019) Integrated records of environmental change and evolution challenge the Cambrian explosion. *Nature Ecology & Evolution* **3**, 528–38. doi: 10.1038/s41559-019-0821-6.

**Wright VP** (1992) A revised classification of limestones. *Sedimentary Geology* **76**, 177–85. doi: 10.1016/0037-0738(92)90082-3.

**Wu YW, Tian H, Li J, Li TF and Ji S** (2021) Reconstruction of oceanic redox structures during the Ediacaran-Cambrian transition in the Yangtze Block of South China: Implications from Mo isotopes and trace elements. *Precambrian Research* **359**, 106181. doi: 10.1016/j.precamres.2021.106181.

**Xi ZD, Tang SH, Zhang SH, Lash GG and Ye YP** (2022) Controls of marine shale gas accumulation in the eastern periphery of the Sichuan Basin, South China. *International Journal of Coal Geology* **251**, 103939. doi: 10.1016/j.coal.2022.103939.

**Yang MH, Zuo YH, Fu XD, Qiu L, Li WZ, Zhang JY, Zheng ZY and Zhang JZ** (2022) Paleoenvironment of the Lower Ordovician Meitan Formation in the Sichuan Basin and adjacent Areas, China. *Minerals* **12**, 75. doi: 10.3390/min12010075.

**Yang W, Xie WR, Wei GQ, Liu MC, Zeng FY, Xie ZY and Jin H** (2012) Sequence lithofacies paleogeography, favorable reservoir distribution and exploration zones of the Cambrian and Ordovician in Sichuan Basin, China. *Acta Petrolei Sinica* **33**, 21–34 (in Chinese with English abstract). doi: 10.7623/syxb2012S2003.

**Zeng HL, Zhao WZ, Xu ZH, Fu QL, Hu SY, Wang ZC and Li BH** (2018) Carbonate seismic sedimentology: a case study of Cambrian Longwangmiao Formation, Gaoshiti-Moxi area, Sichuan Basin, China. *Petroleum Exploration and Development* **45**, 830–9. doi: 10.1016/S1876-3804(18)30086-7.

**Zhai GY, Li J, Jiao Y, Wang YF, Liu GH, Xu Q, Wang C, Chen R and Guo XB** (2019) Applications of chemostratigraphy in a characterization of shale gas Sedimentary Microfacies and predictions of sweet spots—taking the Cambrian black shales in Western Hubei as an example. *Marine and Petroleum Geology* **109**, 547–60. doi: 10.1016/j.marpetgeo.2019.06.045.

**Zhai LN, Wu CD, Ye YT, Zhang SC and Wang YZ** (2018) Fluctuations in chemical weathering on the Yangtze Block during the Ediacaran–Cambrian transition: Implications for paleoclimatic conditions and the marine carbon cycle. *Palaeogeography, Palaeoclimatology, Palaeoecology* **490**, 280–92. doi: 10.1016/j.palaeo.2017.11.006.

**Zhang K, Song Y, Jiang S, Jiang ZX, Jia CZ, Huang YZ, Wen M, Liu WW, Xie XL, Liu TL, Wang PF, Shan CA and Wu YH** (2019) Mechanism analysis of organic matter enrichment in different sedimentary backgrounds: a case study of the Lower Cambrian and the Upper Ordovician-Lower Silurian, in Yangtze region. *Marine and Petroleum Geology* **99**, 488–97. doi: 10.1016/j.marpetgeo.2018.10.044.

**Zhang PY, Wang YL, Zhang XJ, Wei ZF, Wang G, Zhang T, Ma H, Wei JY, He W, Ma XY and Zhu CX** (2022) Carbon, oxygen, and strontium isotopic and elemental characteristics of the Cambrian Longwangmiao formation in South China: Paleoenvironmental significance and implications for carbon isotope excursions. *Gondwana Research* **106**, 174–90. doi: 10.1016/j.gr.2022.01.008.

**Zhang R, Kravchinsky VA, Zhu RX and Yue LP** (2010) Paleomonsoon route reconstruction along a W–E transect in the Chinese Loess Plateau using the anisotropy of magnetic susceptibility: summer monsoon model. *Earth and Planetary Science Letters* **299**, 436–46. doi: 10.1016/j.epsl.2010.09.026.

**Zhang SC, He K, Hu GY, Mi JK, Ma QS, Liu KY and Tang YC** (2018) Unique chemical and isotopic characteristics and origins of natural gases in the Paleozoic marine formations in the Sichuan Basin, SW China: isotope fractionation of deep and high mature carbonate reservoir gases. *Marine and Petroleum Geology* **89**, 68–82. doi: 10.1016/j.marpetgeo.2017.02.010.

**Zhang YF, Hu CL, Wang M, Ma MF, Wang XM and Jiang ZX** (2018) A quantitative sedimentary model for the modern lacustrine beach bar (Qinghai

Lake, Northwest China). *Journal of Paleolimnology* **59**, 279–96. doi: 10.1007/s10933-016-9930-2.

**Zhang YF, Hu CL, Wang XM, Wang M, Jiang ZX and Li JJ** (2017) An improved method of laser particle size analysis and its application in identification of lacustrine tempestite and beach bar: an example from the Dongying Depression. *Journal of Earth Science* **28**, 1145–52. doi: 10.1007/s12583-016-0930-1.

**Zhang YY, Li QJ, Li Y, Kiessling W and Wang JP** (2016) Cambrian to lower Ordovician reefs on the Yangtze platform, South China Block, and their controlling factors. *Facies* **62**, 1–18. doi: 10.1007/s10347-016-0466-8.

**Zhang YY, Li Y, Wang G and Munnecke A** (2017) Windward and leeward margins of an Upper Ordovician carbonate platform in the Central Tarim Uplift, Xinjiang, northwestern China. *Palaeogeography, Palaeoclimatology, Palaeoecology* **474**, 79–88. doi: 10.1016/j.palaeo.2016.12.040.

**Zhao DF, Hu G, Wang LC, Li F, Tan XC, She M, Zhang WJ, Qiao ZF and Wang XF** (2020) Sedimentary characteristics and origin of dolomitic ooids of the terminal Ediacaran Dengying Formation at Yulin (Chongqing, South China). *Palaeogeography, Palaeoclimatology, Palaeoecology* **544**, 109601. doi: 10.1016/j.palaeo.2020.109601.

**Zhao FY, Hu CL, Han CC, Dong YQ and Yuan QX** (2023) Paleocurrent and paleowind direction reconstruction research progress and perspectives: a review. *Australian Journal of Earth Sciences*. Accepted.

**Zhao WZ, Shen AJ, Zhou JG, Wang XF and Lu JM** (2014) Types, characteristics, origin and exploration significance of reef-shoal reservoirs: a case study of Tarim Basin, NW China and Sichuan Basin, SW China. *Petroleum Exploration and Development* **41**, 283–93. doi: 10.1016/S1876-3804(14)60034-3.

**Zhao WZ, Wei GQ, Yang W, Mo WL, Xie WR, Su N, Liu MC, Zeng FY and Wu SJ** (2017) Discovery of Wanyuan-Dazhou Intracratonic Rift and its significance for gas exploration in Sichuan Basin, SW China. *Petroleum Exploration and Development* **44**, 697–707. doi: 10.1016/S1876-3804(17)30081-2.

**Zheng SC, Clausen S, Feng QL and Servais T** (2020) Review of organic-walled microfossils research from the Cambrian of China: implications for global phytoplankton diversity. *Review of Palaeobotany and Palynology* **276**, 104191. doi: 10.1016/j.revpalbo.2020.104191.

**Zhou XW, Jiang ZX, Quaye JA, Duan Y, Hu CL, Liu C and Han C** (2018) Ichnology and sedimentology of the trace fossil-bearing fluvial red beds from the lowermost member of the Paleocene Funing formation in the Jinhu Depression, Subei Basin, East China. *Marine and Petroleum Geology* **99**, 393–415. doi: 10.1016/j.marpetgeo.2018.10.032.

**Zhou Y, Yang FL, Ji YL, Zhou XF and Zhang CH** (2020) Characteristics and controlling factors of dolomite karst reservoirs of the Sinian Dengying Formation, central Sichuan Basin, southwestern China. *Precambrian Research* **343**, 105708. doi: 10.1016/j.precamres.2020.105708.

**Zhu DY, Zhang DW, Liu QY, Xing FC, He ZL, Zhang RQ and Liu ZH** (2018) Formation mechanism of dolomite reservoir controlled by fourth-order sequence in an evaporated marine environment–an example from the lower Ordovician Tongzi Formation in the Sichuan Basin. *Energy Exploration & Exploitation* **36**, 620–44. doi: 10.1177/0144598717736630.

**Zhu RX, Liu QS and Jackson MJ** (2004) Paleoenvironmental significance of the magnetic fabrics in Chinese loess-paleosols since the last interglacial (< 130 ka). *Earth and Planetary Science Letters* **221**, 55–69. doi: 10.1016/S0012-821X(04)00103-7.

**Zhu YQ, Chen GS, Liu Y, Shi XW, Wu W, Luo C, Yang X, Yang YR and Zou YH** (2021) Sequence stratigraphy and lithofacies paleogeographic evolution of Katian Stage–Aeronian Stage in southern Sichuan Basin, SW China. *Petroleum Exploration and Development* **48**, 1126–38. doi: 10.1016/S1876-3804(21)60096-4.

**Zou H, Fang Y, Zhang ST and Zhang Q** (2017) The source of Fengjia and Langxi barite–fluorite deposits in southeastern Sichuan, China: evidence from rare earth elements and S, Sr, and Sm–Nd isotopic data. *Geological Journal* **52**, 470–88. doi: 10.1002/gj.2779.